Biocorrosion on nanofilms induces rapid bacterial motions via iron dissolution

Marion Lherbette, Christophe Regeard, Christian Marliere, Eric Raspaud

Biocorrosion on nanofilms induces rapid bacterial motions via iron dissolution

Marion Lherbette,[1] Christophe Regeard,[2] Christian Marlière,[1] Eric Raspaud[1]*

[1] Université Paris-Saclay, CNRS, Laboratoire de Physique des Solides, 91405, Orsay, France.
[2] Université Paris-Saclay, CEA, CNRS, Institute for Integrative Biology of the Cell (I2BC), 91198, Gif-sur-Yvette, France.

*To whom correspondence should be addressed.

Email: eric.raspaud@universite-paris-saclay.fr

Abstract

Stability and reactivity of solid metal or mineral surfaces in contact with bacteria are critical properties for development of biocorrosion protection and for understanding bacteria - solid environmental interactions. Here, we opted to work with nanosheets of iron nanolayers offering arbitrarily large and stable areas of contact that can be simply monitored by optical means. We focused our study on the sediments' bacteria, the strain *Shewanella oneidensis WT* MR-1, that served as models for previous research on electroactivity and iron-reduction effects. Data show that a sudden uniform corrosion appeared after an early electroactive period without specific affinities and that iron dissolution induced rapid bacterial motions. By extending the approach to mutant strains and three bacterial species, we established a correlation between corrosion onset and oxygen-depletion combined with iron reduction and demonstrated bacterial's extraordinary ability to transform their solid environments.

Main Text

Introduction

Iron is an abundant element found mostly in the two Fe(II) and Fe(III) states in the Earth's crust. Like most living cells that internalize (assimilate) iron for their optimal functioning (homeostasis), some prokaryotic organisms, like the dissimilatory metal-reducing bacteria are also able to utilize environmental and external iron for their own respiration. Cells have adopted different evolutionary strategies to exploit sources of iron in which low solubility at neutral pH reduces availability.[1] Reactivity and stability of interfacial mineral nanolayers are therefore crucial properties involved in the regulation of life evolution in soils and in different processes of nanomineralogy and nanogeoscience.[2,3]

Corrosion is driven by multiple electrochemical reactions on metal surfaces and nanocoatings are among the current approaches of nanotechnology to prevent reactions. "Microbially Influenced Corrosion" (MIC) refers more specifically to the corrosion involving microorganisms.[4–6] Given the variety of microbes, metals and media, MIC involves a myriad of interactions, chemical reactions and mechanisms.[5,7] As microorganisms actively change the local physical/chemical state of solid metal and its surrounding liquid medium, their presence is most often associated with localized pitting corrosion (see [7–9] and references therein). Microorganisms catalyze (initiate/accelerate) local corrosions, separating spatially reduction from oxidation sites along the metal surface. This type of corrosion completely differs from unlocalized corrosion, another well-known type of corrosion. In the latter case, the metal surface degrades uniformly and homogeneously. Though being the subject of extensive research for more than a century ([10] and the references herein[11]), fundamental questions relating to MIC remain unanswered.[5] In particular, little is known about the early steps that initiate corrosion. Traditional models consider degradation kinetics as governed by chemical diffusion and reaction laws. This would imply a quasi-immediate initiation of degradation once bacteria or biofilms are in contact with bare metal.[12,13] However, an effective barrier, an oxide layer that protects the underlying metal from exposure to water and corrosive substances, can cover the metal. Bacteria would have to damage this protection to break down the passivity layer. Therefore, the early steps remain difficult to predict and observe experimentally at the micrometer scale. For instance, light reflection and absorption by the metal hinder direct observation of bacteria (see for instance [14–16] and references herein); the alternative scanning electron microscopy has been recently proposed.[17]

Here, we work with nanosheets (or nanofilms) composed of iron nanolayers (Fig.1A). Reactivity and stability of the semi-transparent nanofilm are studied in the presence of bacteria at the macro and microscale levels. Being anaerobic facultative and serving as models in recent research, the wild type Iron Reducing Bacteria (IRB) *Shewanella oneidensis* MR1 are diluted in a rich static liquid medium that favors its growth. Hence, we report one of the first continuous studies of biocorrosion from its initiation to complete dissolution of the metal. Metal and bacteria were visualized with an optical microscope and analyzed *in situ* directly in the liquid medium. Figure 1B displays bacteria that clearly depart from the substrate background in the presence (left) and absence of iron (right panel). Dissolution of the iron substrate increased the transmitted light and image brightness, while bacteria brought clearly distinctive dark objects to the images in the phase-contrast mode. Observations and image analyses were completed with macroscopic optical and electrical measurements capable of recording nanometer thinning and degradation kinetics, together with microscale measurements of pH and oxygen (O_2) concentrations. The quantitative findings issued from experiments on *Shewanella oneidensis* (mostly), *Escherichia coli* and *Lactobacillus plantarum* (recently renamed *Lactiplantibacillus plantarum*[18]) suggest a positive, temporal correlation between corrosion onset and oxygen depletion combined with iron reduction.

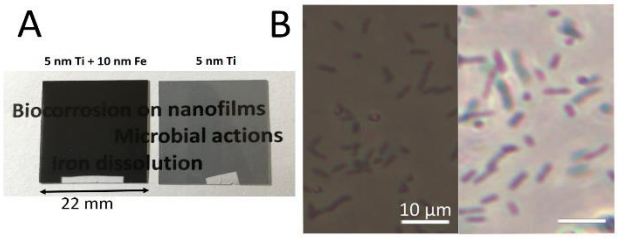

Figure 1. Iron nanofilms. (A) Pictures of grey and semi-transparent nanofilm thermally evaporated on glass coverslips. A titanium prelayer (right coverslip), 5 nm thick, warranted an efficient adhesion of the 10 nm thick iron nanofilm in some samples (left coverslip). (B) Bacteria localized at the metal nanofilm surface (left picture) or on the glass (right picture) were captured using an inverted phase contrast microscope.

Results and Discussion

Iron nanosheets and their surface characterization

The partially transparent metallic film consists of a 10 nm thick iron layer, thermally evaporated, either directly on a microscope glass coverslip or most often on a pre-evaporated 5 nm titanium layer, a typical layer that provides an effective adhesion onto the glass. We verified that the presence or lack of this Ti adhesion layer did not alter the results presented here. Note that iron nanofilm or nanosheet is also termed “ultrathin film” in the literature. Different physical and chemical techniques (optical, electrical, mechanical and spectroscopic) were used to characterize nanofilm, in particular its surface. Being a good compromise, 10 nm of thickness ensures the nanofilm: (1) is transparent (thin) enough to perform optical measurements using an inverted microscope in phase contrast mode, and to record variations of the transmitted light over a large range of light intensity values (as shown in *SI appendix,* Fig.S1 A); (2) is thick enough to be composed of a solid Fe[0] layer

that shares common features with macroscopic Fe[0] bulk metal in terms of chemical state and electrical properties as shown later and in *SI Appendix,* Fig. S1 B. Atomic Force Microscopy (AFM) allowed us to characterize the nanofilm topography and to establish the presence of a perfectly uniform and smooth (or nanorugose) surface over the micrometer scale of bacteria (*SI appendix,* Fig. S1 C-D). The chemical state of all atomic elements across the nanofilm surface was then characterized by X-ray Photoelectron Spectrometry (XPS). Detailed analyses are described in *SI Appendix,* Fig. S2 and revealed the presence of oxygen only at the surface. Hence, the XPS experiments clearly demonstrate that a uniform nanolayer *i.e.* a mostly oxidized iron heterostructure (predominantly composed of Fe(III)) covers the underlying bulk solid metal of the nanofilms; for simplicity, in the subsequent text, this layer will be referred as an oxide layer. These results are in agreement with the nanocoating properties reviewed in [19] and with [20, 21] in which similar nanofilms were studied and where the oxidized iron nanolayers overlaying the Fe(0) metal were found non-crystalline and about 3 nm thick.

A sudden uniform degradation and a concomitant rise in electric current

Inverted optical microscopy was utilized to observe *in situ* nanosheet degradation at the micron scale in static mode, i.e. without liquid flux. Once bacteria were inoculated at time $t = 0$, we performed real time observations in phase-contrast mode and recorded image sequencing every 5 or 10 minutes. In a first attempt, grey values of each pixel on every image were averaged and then analyzed for each sequence; detailed pixel-by-pixel analyses will be presented in subsequent sections. As shown in *SI Appendix,* Fig. S3, the image brightness analyses reveal without ambiguity a uniform and homogeneous corrosion and an intriguing nonmonotonic variation, suggestive of the existence of a sudden corrosion onset.

Specific, self-designed macroscopic experiments of optical transmission were performed to quantitatively measure corrosion kinetics. In Figure 2A, photodiode signals recorded from three samples are plotted as a function of time – high signal indicating high light level. The first two samples correspond to two reference samples: bacteria alone without nanofilm (green), and nanofilm alone without bacteria in the sterile culture medium (blue). In the former case, the signal decreased monotonically with time (green) due to bacterial growth and consequently, to the increasing turbidity of the liquid culture; the corresponding optical density is graduated on the right axis. In the latter curve (blue-filled circles), the signal consistently remains low (about 3.5 volts in Fig. 2A) over time, indicating constant light absorption and no detectable degradation when immersing the nanofilm into a sterile liquid medium. Figure 2A presents a typical recording (red-filled circles) when bacteria are injected and mixed at time $t = 0$ in a dish containing the liquid medium and the iron nanofilm coverslip. Data variation was not monotonic as suspected previously and three phases are clearly distinguishable in Fig. 2A: 1) an initiation phase without any signal variation that lasted a few hours; 2) a degradation phase during which the signal increased and 3) a post-degradation phase when the signal decreased as it did in the bacterial reference sample due to bacterial growth. Corrosion kinetics are extracted from the signal using calibration curves and removing the bacterial contribution. In Figure 2B, the nanofilm thickness is shown as a function of time. At a nanometer resolution, a spatial resolution was optically attainable thanks to the exponential dependence of light absorption with thickness and to the high absorption coefficient of iron (*SI Appendix,* Fig. S1 A). The corrosion onset appeared suddenly at $t = t_{onset}$ and followed a complete metal dissolution within one to two hours. The corrosion rate rose abruptly, reached a constant value equal to 11 +/- 3 nm/h (or equivalently 0.10 mm/y) – a value averaged over all sample values (*SI Appendix,* Corrosion rates and the suspected abiotic corrosion) - and then decreased when

approaching the last metal layers. This value agrees with the data reported in the literature (read for instance [22]).

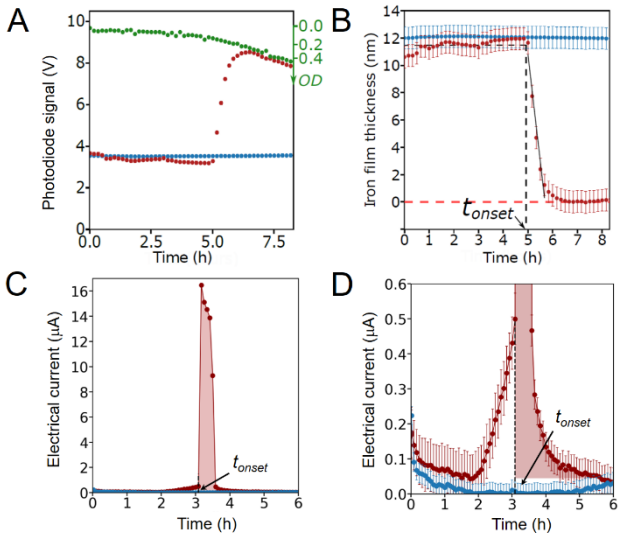

Figure 2. Temporal degradation of a nanofilm as detected by a photodiode mounted in an optical macroscopic setup (A). The calibrated setup allowed us to measure the transmitted light signal (A) and to determine iron film thickness as a function of time (B). Multiplying bacteria also contributed to turbidity as shown by the signal variation on a reference sample without iron nanofilm (green-filled circles in (A)); Optical Density (*OD*) of the bacterial solution is graduated on the right axis. Initial bacteria concentration, *OD* = 0.003. The optical signal was constant when immersing iron nanofilm into liquid medium without bacteria (blue-filled circles in (A-B)), while it varied in the presence of both bacteria and nanofilm (red-filled circles). Metal corrosion onset appeared suddenly at $t = t_{onset}$.. Color code in the following figures: green (*Shewanella* alone), blue (nanofilm alone), red (*Shewanella* + nanofilm). (C-D) Electrical current as measured during metal degradation when connecting the iron nanofilm (without Ti layer) to an ammeter and a platinum counter-electrode half-immersed from the top of the liquid sample. With the sample being placed on the optical setup, we were able to measure both electrical and optical signals *in situ* simultaneously. Metal dissolution also appeared suddenly. Initial *OD* = 0.03. (C) As measured by the ammeter, relatively large electron flows (more than 10 microAmperes) were produced concomitantly with metal dissolution (red-filled circles). Note that only absolute values of the negative current are plotted in (C-D). Summing the intensity values in a definite integral (red area) leads us to estimate a total charge flowing through the circuit equal to 0.045 C, close to 0.066 C, the charge expected when roughly assuming one electron transfer per dissolved iron atom. (D) The magnified figure reveals early variations of the low current values before optical semi-transparency began to change suddenly at $t = t_{onset}$.

As electrochemical reactions and consecutive electron transfers induce iron dissolution, it is possible to detect the corrosion event by measuring electric current. Figure 2C displays the results recorded on one sample with (red) and one without bacteria (absolute values, blue-filled circles). The electric current of the latter remained constant and low (< 0.2 µA) over time. By contrast, in the presence of bacteria, a degradation phase of high current level (> 0.5 µA) was found to surround both the initiation and post-degradation phases of low current level. The sudden nanofilm thinning (optically measured on the same sample) that defined $t = t_{onset}$ was found concomitant with the sudden rise in electric current. The directional current flow allowed us to conclude that electrons were flowing from the iron nanofilm to the platinum counter-electrode, suggesting an anodic metal dissolution – as would be expected for a "strict" corrosion – coupled to a reduction at the counter-electrode; the nanofilm degradation is therefore corrosion. As seen in Fig. 2C, the current suddenly reaches 15-20 microamperes and then drops by 90 percent at the end of the thinning

process. The magnified Figure 2D shows the small current values for clarity and displays a slow and weak increase of the electric current one hour before the corrosion onset. This period of early weak electroactivity which lasted between 30 minutes and 1 hour and 30 minutes – noted ½ h and 1 h 30 in this study – depending on the sample, was not detectable from optical signals that instead, remained constant, suggesting no change in the solid Fe(0) layer thickness during this electroactive period.

Next, we measured the Open Circuit Potential (*OCP*) using a voltmeter connected to the nanofilm and to an Ag/Ag-Cl counter-electrode immersed in the liquid medium (*SI Appendix,* Fig. S4). Reference samples exhibited low and constant voltage values (- 60 +/- 40 mV), indicating a relatively stable passive state of the oxidized iron nanolayers over long periods. By contrast, sudden rises in negative *OCP* values associated with the sudden rise in current were clearly observed at $t = t_{onset}$. An abrupt drop at about -600 mV signals the passivity breakdown. Corrosion onset quickly followed an early progressive decrease to -225+/-60 mV (on average) signaling early progressive surface modifications.

In order to interpret these data, we measured the electrical properties of a bulk iron sheet (0.1 millimeter-thick) under the same conditions. The sheet was previously exposed to ambient air and humidity and showed no visible signs of rust or oxidation. Just after its immersion into sterile liquid medium (without bacteria), the sheet started to corrode. A current of 10-20 μA (vs Pt) and a corrosion voltage of -650 mV (vs Ag/AgCl) were detected quasi-immediately and over long periods (*SI Appendix,* Fig. S5). These readings indicate the rapid instability of the oxide covering of the bulk thick metal compared to the stability of the oxidized iron overlaying the Fe(0) nanolayers and confirms that the nanocoatings are able to reduce the effect of a corrosive environment.[19] Furthermore, the similar *OCP* values suggest that nanofilm with bacteria corrodes like thick metal without bacteria. In both cases, the electrochemical reactions could occur at the solid Fe(0) metal-liquid medium surface and drive the corrosion without the possible regeneration of an oxide layer sufficiently passive to protect the underlying metal. These reactions lead to the oxidation of the metal and its progressive dissolution together with the electron flow from the oxidized metal, through the electrical wire and up to the platinum electrode where reduction occurred (*SI Appendix*, Corrosion rates and the suspected abiotic corrosion).

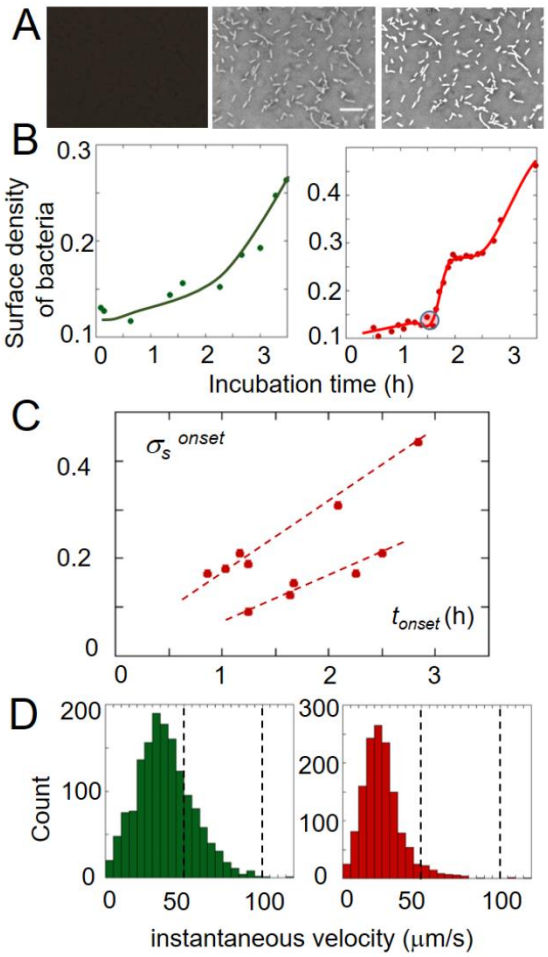

Figure 3. Surface density and dynamics of bacteria in contact with, or nearby, the iron nanofilm as detected by digital image processing and analysis. (A) Bacteria are clearly visible on the center picture when processing thresholding and renormalization of the initial left image. Scale bar = 20 μm. On the right image, bacterial areas, as detected by image segmentation and binarization, are white-colored and superimposed over bacteria observed on the original middle image. Initial *OD* = 0.07. (B) Surface densities of bacteria, calculated from the white areas and denoting the area covered by cells per unit area, are plotted as functions of time. Bacterial areas of two representative samples were measured: a reference sample where bacteria were in contact with the glass coverslip (the left plot, dark green-filled circles); one sample with iron nanofilm exhibiting a different density curve (the right plot, red-filled circles). The time t_{onset} of corrosion onset, deduced from the mean grey value, is marked by a semi-transparent colored disk. Curved continuous lines are simply guides for the eyes. Initial *OD* = 0.07. (C) The bacterial surface density (per unit area) measured at $t = t_{onset}$ on different samples is plotted as a function of t_{onset} (details in Figure S6). Data could split in two clusters with a positive linear correlation, as indicated by the two dashed red lines. (D) Histograms of the bacterial instantaneous velocity deduced from tracking: 1) left histogram (green bars): velocities of long runs when bacteria – freshly removed from the incubator shaker and diluted – swam in the oxygenated liquid culture; 2) right histogram (red bars): velocities of bacterial rapid motions and short runs observed just after corrosion onset. The weak difference in the mean velocity might come from the constrained environment where bacteria were densely moving near the metallic surface; a decreased velocity was caused by collisions with one another.

Surface density, localization and dynamics of bacteria

While the corrosion onset time was easily extracted from the mean grey values, detailed and quantified studies of bacteria density and dynamics require more advanced image processing. The one-looped *SI Appendix,* Movie S1 shows six sequences of 50 images recorded every 30-50 ms. Figure 3A displays an example of image processing leading to the Movie S1; starting from the initial dark picture on the left, a renormalization using thresholds led to the middle picture where grey levels have been inverted. Movie S1 provides considerable information on bacterial shape, dynamics and surface distribution before and after the corrosion onset. A first visual inspection indicates that bacteria were homogeneously distributed on the surface over time. Few filamentous cells and no biofilm clusters were visible within the four-hour period that followed the inoculation – a pellicular biofilm being seen 12-24 h later. Instead, individual growing cells were the most abundant population regardless of the samples.

Image analyses allowed us to unambiguously determine the bacterial surface density (per unit area), the area fraction calculated by dividing the area covered by the detected bacteria on each image by the total image area (*SI Appendix,* Fig. S6). Figure 3B shows the surface density of two incubated bacterial samples, one without (left) and one with metal nanofilm (right plot). Overall, no precise value nor unique law governing cell numbers at the surface was observed and their global number weakly increased with incubation time. However, the cells' density of some samples presented a sudden non-monotonic change just after corrosion onset; this non-monotonic change will be discussed in the next paragraph. Depending on the sample (*SI Appendix,* Fig. S6), the corrosion process began at very different t_{onset} values (from 1 to 3 hours) and at very different surface density values, further noted σ_s^{onset} (from 10 to 45 %).As shown on the same scatter plot in Figure 3C, data (t_{onset}, σ_s^{onset}) may form two unexpected distinct groups that are aligned to two distinct oblique and quasi-parallel straight lines, meaning two clusters have linear positive correlation; many experiments will be needed to distinguish the possible correlation.

The two most striking observations in *SI Appendix*, Movie S1 are (1) the absence of motility of some cells standing over the metal nanofilm – immobilized and motionless cells are named sessile bacteria in the following text – associated with the early period of weak electroactivity; (2) in contrast, the presence of many single and rapidly moving bacteria appearing just after the corrosion onset. (1) A first quantitative and detailed sessility analysis, in terms of localization function, is proposed in *SI Appendix*, Figure S7 and it reveals an almost complete renewal or surface regeneration of bacteria during the initiation phase. Bacteria located at or near the metal or glass surface were not attached strongly enough to the metal to remain localized on the same site. Many newly incoming bacteria recolonized the surface during the whole phase. A similar lack of cells' affinity for glass and for solid metal clearly appeared. (2) By contrast, the previous non-monotonic change in surface density quantified a sudden influx of rapidly moving bacteria seen in *SI Appendix,* Movie S1. The iron, being progressively released and solubilized as soon as the corrosion started, generated a local iron concentration gradient that was most likely detected by bacteria, directing their motions toward the rich region surrounding the dissolving nanofilm, as already reported in [23,24] and in [25] for *Geobacter Metallireducens*. Every bacterium was highly dynamic and all local motions were rapid. A histogram of the instantaneous velocities is plotted on the right side of Fig. 3D and the mean velocity value is found to be equal to 25 +/-13 μm/s. This value is close to 38 +/-18 μm/s, the mean velocity value that was measured when diluted *S. oneidensis* performed long runs in freshly oxygenated medium (histogram on the left).

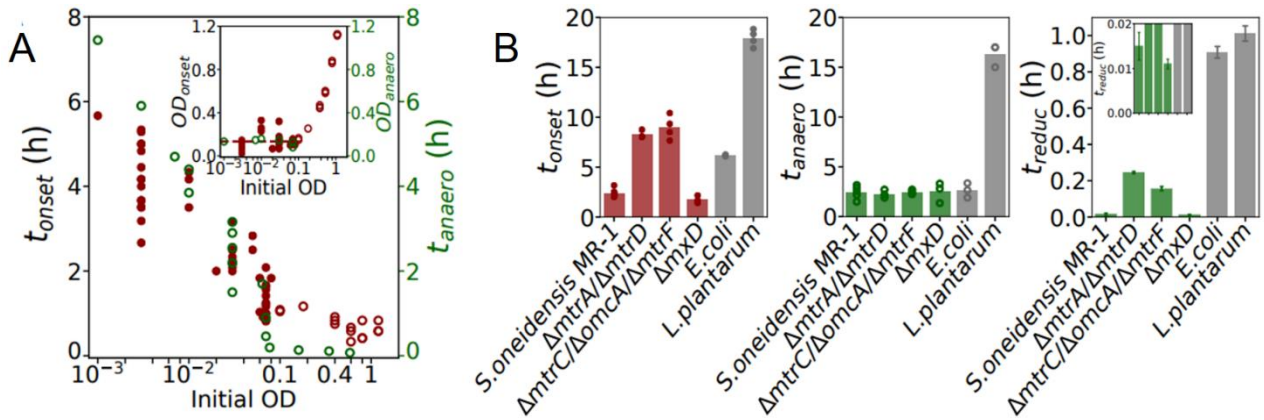

Figure 4. Environmental and microbiological factors influencing the time of corrosion onset. (A) Duration of the initiation phase, as defined by t_{onset} and reported on the left vertical axis, depended on the initial bacterial concentration, which was quantified by the initial Optical Density (*OD*) of the liquid culture. In the insert, the mean macroscopic OD_{onset} values reached at $t = t_{onset}$ are plotted on the left ordinate axis as a function of the initial *OD*. Comparison between t_{onset} and t_{anaero} or between OD_{onset} and OD_{anaero} with t_{anaero} and OD_{anaero} (graduated on the right vertical axes and denoting, respectively, the time and mean Optical Density needed to reach a strict anaerobic environment nearby the metal nanofilms). Two concentration regimes clearly appeared: 1) when the samples were already highly concentrated, two constant periods of incubation 45 +/- 15 minutes and, a few minutes, irrespective of the samples, were required to observe corrosion (red-empty circles) and full-O_2 depletion (green-empty circles) respectively. 2) when starting from a diluted bacterial concentration, bacteria grew until they reached a constant bacterial concentration (0.13 +/- 0.06; dashed line in the insert) sufficient enough to enable the transition toward corrosion (red-filled circles) and to fully and locally deplete oxygen (green-empty circles). (B) Three characteristic times measured or calculated for four *S. oneidensis* strains (t_{onset}, red-filled circles and bars; t_{anaero} and t_{reduc}, green-filled circles and bars) and for the two other species, *E. coli* WT and *L. plantarum* (grey-filled circles and bars). Here t_{onset} and t_{anaero} are the two first characteristic times directly measured on all the strains and species. . Initial *OD* = 0.03. Knowing that the liquid medium contains about 10 μM of soluble iron (more exactly 17 μM),[27] the third characteristic time corresponds to the time t_{reduc} required for reducing 10 μM of soluble iron(III) at a k_{reduc} rate. Kinetics of iron(III) reduction were quantified separately in order to determine the different k_{reduc} values of the reduction rate; data are reported on *SI Appendix*, Fig. S10.

Iron reduction in a local anaerobic environment

We varied environmental and microbiological parameters in order to determine the triggering events that stimulated passivity breakdown. Initial bacterial densities were first modified and, regardless of the initial bacterial concentrations, corrosion was found uniform and sudden. All t_{onset} values are plotted in a semi-logarithmic graph in Figure 4A in which two concentration regimes appear. In the first regime, at high initial *OD* values (> 0.1), the t_{onset} values are independent of the initial conditions and on average, corrosion began at t_{onset} = 45 +/- 15 minutes. In the second regime, when initial cells were highly diluted (*OD* < 0.1), passivity breakdown was delayed; in Fig. 4A, all t_{onset} values globally decrease linearly following a logarithmic scale relationship which suggests a global bacterial growth effect. Monitoring in parallel the turbidity of bacterial samples without nanofilm allowed us to determine the liquid solution *OD* values reached at any time and in particular at $t = t_{onset}$ – assuming that the nanofilm did not modify the bacterial growth in the bulk. The corresponding *OD* values reached at $t = t_{onset}$, termed OD_{onset}, are plotted as a function of the initial *OD* in the Figure 4A insert; we found an average value equal to OD_{onset} = 0.13 +/-

0.06 (equivalent to 10^8 colony-forming-units/ml). Hence, during the early initiation phase, we know that, on one hand, bacteria multiplied up to a minimum concentration indicating a potential quorum sensing effect and/or activation of a different metabolic pathway. On the other hand, some progressive electrochemical reactions modify the oxide layer and its environment. Additional experiments indicated that direct bacteria-nanofilm contacts were absolutely needed during this early initiation phase (*SI Appendix*, Separated compartments). This result can be related to other reports obtained in conditions relevant for biofilms in the future.[26]

As Iron Reducing Bacteria, like *S. oneidensis,* are known to respire insoluble metals only under anaerobic condition, we first monitored O_2 levels of the bacterial microenvironment surrounding a glass coverslip using a microsensor in samples of different initial concentrations. *SI Appendix*, Figure S8 depicts three oxygen-depletion kinetics. As suspected, oxygen was locally depleted within 5 minutes to 6 hours following the inoculation depending on the initial bacteria concentration. These t_{anaero} sample values are reported in Fig.4A and are compared to the t_{onset} values. Interestingly, both values are very similar in the second concentration regime (low initial *OD* values < 0.07) supporting the idea of a strong correlation between anaerobic conditions and corrosion onset. In the first concentration regime (initial *OD* values > 0.07-0.1) however, values differ: if oxygen was rapidly depleted in less than 10 minutes, 45 minutes were required to initiate corrosion. Thus, the results indicate that metal corrosion observed on all samples occurred in an almost strictly anaerobic environment where iron respiration may have occurred and an additional period of anaerobic incubation was needed to trigger the degradation. If this additional period was not sufficiently long enough for cells to duplicate, it did allow them to express the necessary genes involved in the interaction with the iron oxide surface. This additional period prior to the corrosion onset is consistent with the duration of the early electroactive period noticed before. At $t = t_{anaero}$, the bacterial concentration of a few samples OD_{anaero} in the second regime was also measured using a spectrophotometer and the results are shown in the Fig.4A insert. Again, OD_{onset} and OD_{anaero} values are identical, demonstrating the need for reaching a minimal and global bacterial density to fully deplete oxygen from the local environment of metal nanofilms and to enable their passivity breakdown.

We further noticed a significant delay in corrosion onset upon addition of soluble extra-iron Fe(III) to the medium (*SI Appendix*, Figure S9), reinforcing the importance of microbial respiration in the triggering event and interplay between soluble and insoluble iron reduction. As the culture medium itself contained an initial amount of soluble iron molecules (of the order of 10-20 μM concentration, too low to be measured in our conditions[27]), these initial soluble iron were then suspected to interplay with the reduction of the insoluble Fe(III) oxides located at the nanosheet surface. The reduction kinetics, in itself, was then measured in separate experiments under conditions mimicking the local nanofilms' environment (anaerobic & *OD* = 0.1) and in the presence of soluble Fe(III) ammonium citrate molecules (10 mM); abiotic controls indicated no significant amount of reduced iron. As displayed in *SI Appendix*, Figure S10, a linear fit of the first reduced Fe(II) concentrations vs. time allowed us to determine the reduction rate k_{reduc} and the related time t_{reduc}. This time, t_{reduc} corresponds to the time that would be required for bacteria to reduce the few soluble iron molecules present in the liquid culture (10 μM) at the rate k_{reduc}, i.e. without considering the complex environment of the standing culture in aerobic atmosphere and the limiting diffusion of diluted iron molecules. To summarize, the three different characteristic times (t_{onset}, t_{anaero} and t_{reduc}) determined on *S. oneidensis* WT and on three mutants are reported on three graphs in Figure 4B. The MtrC, OmcA and MtrF decaheme c-type cytochromes (the terminal electron donors within the external membrane) are deprived in the first mutant, impeding the outer traditional electron pathway that reduces iron oxides, while the MtrA and MtrD decaheme c-type cytochromes that facilitate internal electron transfers to the other previous outer membrane cytochromes are

deleted in the second mutant.[28] Mutations significantly delayed reduction time and corrosion onset unlike the mutation of the third mutant unable to synthesize extracellular polysaccharides.[29] This result clearly demonstrates: i) c-cytochromes of the Mtr pathway are implicated in nanofilm corrosion initiation; ii) the two mutants were able to interact with iron using alternative and less efficient pathways, reflecting the extraordinary respiratory versatility of *S. oneidensis*;[30,31] iii) a positive temporal correlation between corrosion onset and soluble iron reduction, the time of corrosion onset being less impacted by the mutations than the reduction time – such a difference might be related to the secretion of extracellular flavins, molecules considered as electron shuttles that preferentially facilitate the reduction of soluble iron rather than insoluble iron;[32,33] iv) the polysaccharide matrix was not implicated in the corrosion process under our short-term experimental conditions.

Finally, the last series of experiments were done on two other facultative anaerobes different from Iron Reducing Bacteria, *Escherichia coli* and *Lactobacillus plantarum*. As reported by Logan *et al.* in a recent review (see also the references herein [34]), *E. coli* is often used as a negative control, non-exoelectrogen i.e. not equipped with the membrane proteins chain permitting external electron transfers (EET). Though not being able to respire external insoluble iron unlike IRB, *E. coli* cells need iron for metabolism like most living cells and few studies discriminate the dissimilation from assimilation processes (see for instance [35]). By contrast, *L. plantarum* is one exception of living cells that do not (or very little) depend on iron[1,36] but do contain genes for EET (not all) as recently reported.[37] Its ability to reduce external soluble Fe(III) was found close to nil (but non nil) and to correspond to the lowest activity across part of the Firmicutes phylum.[37] All results are summarized in Figure 4B and indicate that, although not being as efficient as *S. oneidensis*, both (*E. coli* and *L. plantarum*) enabled the transition toward the corrosion process. Supplementary analyses suggest a passivity breakdown mediated by small secreted soluble compounds like molecular shuttles and byproducts of *E. coli* fermentation rather than direct contacts in agreement with [38] (*SI Appendix*, Separated compartments), and related to the acidic environment of *L. plantarum* (measured using microsensors) (*SI Appendix,* Figure S11).

Note that corrosion rates performed on mutants and on the two other species are shown in (*SI Appendix,* Figure S12) and discussed in (*SI Appendix*, Corrosion rates and the suspected abiotic corrosion).

Hence, transformation and dissolution of environing iron are remarkable common features shared by a number of bacterial species, as suggested by the present experiments and by previous studies (see for instance [34,39]). Our present experiments, based on microscopic observations through an iron nanofilm, allows us to monitor initial stages and to display positive temporal correlations between corrosion onset and oxygen depletion combined with iron reduction. Further detailed studies could permit the identification of mechanisms responsible for passivity breakdown. The early steps of matter transformation, being interfacial, nanometer-thin materials, may offer new insight into elucidating bacterial actions within other processes, such as plastic biodegradation and solid pollutant bioremediation, and new perspectives into nanocoatings capable of improving materials' functionalities.

Materials and Methods

Iron nanofilm processing/preparation. (*SI Appendix, Iron nanofilm processing/preparation*)

AFM measurements. (*SI Appendix, AFM measurements*)

Bacterial strain and growth conditions

Wild type *Shewanella oneidensis* strain MR-1 (LGC Standards), the deleted mutants JG594 (ΔmtrA/ ΔmtrD),[28] JG596 (ΔmtrC/ ΔomcA/ ΔmtrF),[28] and (ΔmxD)[29] were cultured similarly. Single colonies were obtained by isolation from frozen stocks on Luria Broth (LB) agar plates and inoculated into 5mL of liquid LB, shaken for 18 h at 200 rpm at 30°C for overnight cultures. Then, typical dilutions (1:1000) in LB from overnight culture were completed. Most bacteria were picked up at the beginning of the exponential phase when OD ~ 0.1 and then diluted in LB in one of the different culture chambers. The Optical Density (OD) measured at 600 nm provided an estimation of the cell concentration in each sample; OD values were calibrated to colony-forming-units (cfu) by spreading multiple dilutions on agar plates and counting the number of colonies: 1 OD = $7x10^8$ cells/ml. All experiments presented here were done at 23-25°C. At the end of each experiment, culture purity was controlled by analyzing the colonies' morphology obtained after a streaking in an LB plate.

A bottomless and topless culture chamber made of glass-filled PTFE and suitable for use with an inverted microscope (ZEISS Primovert) was designed and machined at the laboratory. After placing and sealing the nanofilm's coverslip at the bottom, the chamber was filled from the top with 2.5 ml of bacterial culture in a sterile cabinet and covered with a classical glass coverslip. Optical and electrical experiments were performed in small Petri dishes (50 x 20 mm), immersing the nanofilm's coverslip to the dish's bottom into 10 ml of liquid culture.

No unexpected or unusually high safety hazards were encountered.

Optical macroscopic measurements. (*SI Appendix, Optical macroscopic measurements)*

Electrical measurements. (*SI Appendix, Electrical measurements)*

Microscopic measurements of pH and oxygen (O_2) concentration. (*SI Appendix, Microscopic measurements of pH and oxygen (O2) concentration*)

Iron Reduction – Ferrozine assay. (*SI Appendix, Iron Reduction – Ferrozine assay*)

Acknowledgments

Authors would like to greatly thank Diana Dragoe for her help in this study. Diana welcomed the authors at the XPS platform at the ICMMO laboratory – CNRS/Paris-Saclay University, initiated them to the techniques and performed the XPS measurements together with the result analyses. Authors would like to thank Prof. Jeffrey A. Gralnick and C. Jourlin-Castelli who kindly provided the mutant *Shewanella* strains (Δ*mtrA*/ Δ*mtrD* and Δ*mtrC*/ Δ*omcA*/ Δ*mtrF*) and Δ*mxD* respectively, and V. Gueneau and J. C. Piard the *Lactobacillus plantarum* strain. We thank all the interns who worked on the bacterial electroactivity (A. Roux, T. Rakotanavo, M. Grandvillain, V. Gueneau, M. Lopez Ortiz, F. Semmer, B. Casteigst, D. Letessier, R. Wild, G. Tornafol, I. Meyre-Baque, F. Baudribos, N. Malhomme, M. Barrault). The authors benefited from the LPS technical assistance (Elinstru, Mécanique, Nano) and especially Jérémie Sanchez, Stephane Cabaret & Marc Bottineau, Sylvie Gautier among others –thanks to all of them- and special thanks to Virginie Bailleux and Laetitia Poncet who helped the authors in the multiple microbiological preparations and performed most of the iron reduction experiments. This study would not be possible without our colleagues. We greatly thank Lydia Couturier and Louis Genain for the grammar checking, english spellings and suggestions. Finally, we greatly thank D. Féron, R. Basséguy and A. Bergel for fruitful discussions and for sharing their expertise. The project initiation has benefited from an early CNRS funding

(PEPS: “Biofilms-biocapteurs-biopiles pour une ingénierie environnementale”). This work is supported by a public grant from the “Laboratoire d’Excellence Physics Atoms Light Mater” (LabEx PALM) overseen by the French National Research Agency (ANR) as part of the “Investissements d’Avenir” program (reference: ANR-10-LABX-0039-PALM) ».

Supporting Information

Supplementary Text

- Corrosion rates and the suspected abiotic corrosion
- Separated compartments
- Iron nanofilm processing/preparation
- AFM measurements
- XPS measurements
- Optical macroscopic measurements
- Electrical measurements
- Microscopic measurements of pH and oxygen (O_2) concentration
- Iron Reduction – Ferrozine assay

Supplementary Figures

- Figure S1: Some physical properties of iron nanofilms
- Figure S2: Spectra of X-ray Photoelectron Spectrometry
- Figure S3: Temporal degradation of a nanofilm as observed by optical microscopy
- Figure S4: Open Circuit Potential measured during the nanofilm degradation
- Figure S5: Electrical signals measured during the bulk iron degradation
- Figure S6: Temporal variations of bacterial surface density
- Figure S7: Cells’ dynamics and sessility analysis
- Figure S8: Kinetics of oxygen (O_2) depletion
- Figure S9: Delay in the corrosion onset upon addition of soluble Fe(III)
- Figure S10: Kinetics of iron(III) reduction
- Figure S11: Temporal variations of local pH
- Figure S12: Corrosion rates

Supplementary Material

- Movie S1: A one-looped and slow motion movie showing six sequences recorded before and during the corrosion

For Table of Contents Use Only

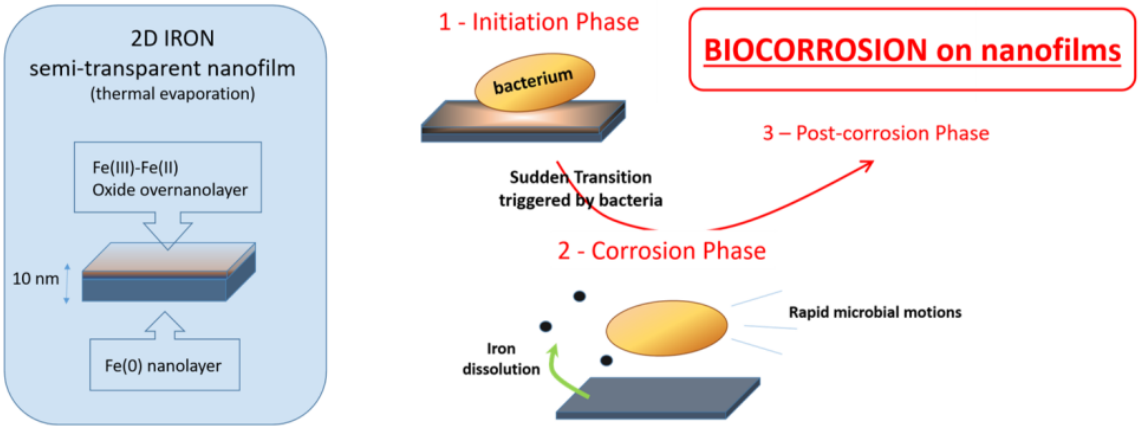

Synopsis:

Biocorrosion on two-dimensional iron semitransparent nanofilms has been measured, and it revealed a sudden transition triggered by bacteria with rapid microbial motions associated with iron dissolution.

References

1. S. C. Andrews, A. K. Robinson, F. Rodríguez-Quiñones, Bacterial iron homeostasis. *FEMS Microbiol. Rev.* 27, 215–237 (2003).
2. M. Ilbert, V. Bonnefoy, Insight into the evolution of the iron oxidation pathways. *Biochim. Biophys. Acta* 1827, 161-175 (2013).
3. M. F. Hochella Jr, S. K. Lower, P. A. Maurice, R. L. Penn, N. Sahai, D. L. Sparks, B. S. Twining, Nanominerals, mineral nanoparticles, and earth systems. *Science* 319, 1631-1635 (2008).
4. H.-C. Flemming, in Microbially Influenced Corrosion of Materials - Scientific and Technological Aspects, E. Heitz, W. Sand, H.-C. Flemming, Eds. (Springer, Heidelberg, 1996), pp. 5–14.
5. B. J. Little, D. J. Blackwood, J. Hinks, F. M. Lauro, E. Marsili, A. Okamoto, S. A. Rice, S. A. Wade, H.-C. Flemming, Microbially influenced corrosion – Any progress? *Corros. Sci.* 170, 108641 (2020).
6. Nace International. 2016. http://impact.nace.org/economic-impact.aspx.
7. Z. Lewandowski, H. Beyenal, in Marine and Industrial Biofouling, H.-C. Flemming, P. S. Murthy, R. Venkatesan and K. E. Cooksey, Eds. (Springer-Verlag, Berlin Heidelberg, 2009), pp. 35-65.
8. H.-C. Flemming, G. G. Geesey, Biofouling and Biocorrosion in Industrial Water Systems (Proceedings of the International Workshop on Industrial Biofouling and Biocorrosion, Stuttgart, 1990).
9. S. B. Borenstein, Microbiologically influenced corrosion handbook (Industrial Press, New York, 1994).
10. W. P. Iverson, Microbial corrosion of metals. Adv. Appl. Microbiol. 32, 1-36 (1987).
11. J. F. D. Stott, What progress in the understanding of microbially induced corrosion has been made in the last 25 years? A personal viewpoint. *Corros. Sci*. 35, 1-4, 667-673 (1993).
12. R. E. Melchers, T. Wells, Models for the anaerobic phases of marine immersion corrosion. *Corros. Sci.* 48, 1791-1811 (2006).
13. A. Marciales, Y. Peralta, T. Haile, T. Crosby, J. Wolodko, Mechanistic microbiologically influenced corrosion modeling- a review. *Corros. Sci.* 146, 99-111 (2019).
14. Y. Wang, G. Cheng, Y. Li, Observation of the pitting corrosion and uniform corrosion for X80 steel in 3.5% NaCl solutions using in-situ and 3D measuring microscope. *Corr. Sci.* 111, 508-517 (2016).
15. B. Yuan, Z. Li, S. Tong, L. Li, C. Wang, In Situ Monitoring of Pitting Corrosion on Stainless Steel with Digital Holographic Surface Imaging. *J. Electrochem. Soc*., 166, C3039 (2019).
16. G. Sander, V. Cruz, N. Bhat, N. Birbilis, On the in-situ characterization of metastable pitting using 316L stainless steel as a case study. *Corros. Sci.* 177, 109004 (2020).
17. L. Iannucci, L. Lombardo, M. Parvis, P. Cristiani, R. Basséguy, E. Angelini, and S. Grassini, paper presented at the 2019 IEEE International Instrumentation & Measurement Technology Conference, Auckland, New Zealand, May 2019.
18. J. Zheng et al., A taxonomic note on the genus *Lactobacillus*: Description of 23 novel genera, emended description of the genus *Lactobacillus Beijerinck 1901*, and union of *Lactobacillaceae* and *Leuconostocaceae*. *Int. J. Syst. Evol. Microbiol*. 004107, 1-77 (2020).
19. D. H. Abdeen, M. El Hachach, M. Koc, M. A. Atieh, Review on the Corrosion Behaviour of Nanocoatings on Metallic Substrates. *Materials*, 12, 210 (2019).
20. M. D. Boamah, E. H. Lozier, J. Kim, P. E. Ohno, C. E. Walker, T. F. Miller III, F. M. Geiger, Energy conversion via metal nanolayers. *Proc. Natl. Acad. Sci. U.S.A* 116, 16210-16215 (2019).

21. D. Faurie-Wisniewski, F. M. Geiger, Synthesis and characterization of chemically pure nanometer-thin zero-valent films and their surfaces. *J. Phys. Chem. C* 118, 23256-23263 (2014).
22. D. Féron, D. Crusset, Microbial induced corrosion in French concept of nuclear waste underground disposal. *Corros. Eng. Sci. and Techn*. 49, 540-547 (2014).
23. H. W. Harris, I. Sanchez-Andrea, J. S. McLean, E. C. Salas, W. Tran, M. Y. El-Naggar, K. H. Nealson, Redox sensing within the genus *Shewanella*. *Front. Microbiol*. 8, 2568 (2018).
24. H. W. Harris, M. Y. El-Naggar, O. Bretschger, M. J. Ward, M. F. Romine, A. Y. Obraztsova, K. H. Nealson, Electrokinesis is a microbial behavior that requires extracellular electron transport. *Proc. Natl. Acad. Sci. U.S.A* 107, 326-331 (2010).
25. S. E. Childers, S. Ciufo, D. R. Lovley, *Geobacter metallireducens* accesses insoluble Fe(III) oxide by chemotaxis. *Nature*, 416, 767-769 (2002).
26. D. P. Lies, M. E. Hernandez, A. Kappler, R. E. Mielke, J. A. Gralnick, D. K. Newman, *Shewanella oneidensis* MR-1 uses overlapping pathways for iron reduction at a distance and by direct contact under conditions relevant for biofilms. *Appl. Environ. Microbiol*. 71, 4414-4426 (2005).
27. H. Abdul-Tehrani et al, Ferritin mutants of *Escherichia coli* are iron deficient and growth impaired, and fur mutants are iron deficient. *J Bacteriol.* 181, 1415–1428 (1999).
28. D. Coursolle, J. A. Gralnick, Modularity of the Mtr respiratory pathway of *Shewanella oneidensis strain MR-1*. *Mol. Microbiol*. 77, 995-1008 (2010).
29. C. Gambari, A. Boyeldieu, J. Armitano, V. Méjean and C. Jourlin-Castelli, Control of pellicle biogenesis involves the diguanylate cyclases PdgA and PdgB, the c-di-GMP binding protein MxdA and the chemotaxis response regulator CheY3 in *Shewanella oneidensis*. *Environ. Microbiol*. 21, 81–97 (2019).
30. M. Breuer, K. M. Rossob, J. Blumberger, Electron flow in multiheme bacterial cytochromes is a balancing act between heme electronic interaction and redox potentials. *Proc. Natl. Acad. Sci. U.S.A.* 111, 611–616 (2014).
31. T. E. Meyer, A. I. Tsapin, I. Vandenberghe, L.de Smet, D. Frishman, K. H. Nealson, M. A. Cusanovich, and J. J. van Beeumen, Identification of 42 possible cytochrome C genes in the *Shewanella oneidensis* genome and characterization of six soluble cytochromes. *OMICS* 8, 57 (2004).
32. S. S. Ruebush, S. L. Brantley, M. Tien, Reduction of soluble and insoluble iron forms by membrane fractions of *Shewanella oneidensis* grown under aerobic and anaerobic conditions. *Appl. Environ. Microbiol.* 72, 2925–2935 (2006).
33. N. J. Kotloski, J. A. Gralnick, Flavin electron shuttles dominate extracellular electron transfer by *Shewanella oneidensis*. *mBio*, 4, e00553-12 (2013).
34. B. E. Logan, R. Rossi, A. Ragab, P.E. Saikaly, Electroactive microorganisms in bioelectrochemical systems. *Nat. Rev. Microbiol.* 17, 307 (2019).
35. B. M. R. Appenzeller, C. Yanez, F. Jorand, J.-C. Block, Advantage provided by iron for *Escherichia coli* growth and cultivability in drinking water. *Appl. Environ. Microbiol.* 71, 5621-5623 (2005).
36. F. Archibald, *Lactobacillus plantarum*, an organism not requiring iron. *FEMS Microbiol. Lett.* 19, 29-32 (1983).
37. S.H. Light et al., A flavin-based extracellular electron transfer mechanism in diverse Gram-positive bacteria. *Nature* 562, 140 (2018).
38. J.B. McKinlay, J.G. Zeikus, Extracellular ion reduction is mediated in part by neutral red and hydrogenase in *Escherichia coli*, *Appl. Environ. Microbiol.* 70, 3467 (2004).
39. D. R. Lovley, Microbial Fe(III) reduction in subsurface environments. *FEMS Microbiol. Rev*., 20, 305–313 (1997).

Supplementary Information for

Biocorrosion on nanofilms induces rapid bacterial motions via iron dissolution

Marion Lherbette, Christophe Regeard, Christian Marlière, Eric Raspaud*

Eric Raspaud

Email: eric.raspaud@universite-paris-saclay.fr

This PDF file includes: (22 pages)

Other supplementary materials for this manuscript include the following:

Movie S1

Supplementary Text

Corrosion rates and the suspected abiotic corrosion

As illustrated in Fig. 2B, the linear function equation that best fits the thinning data points – data issued from the optical signal measurements – allowed us to extract a reaction speed, i.e. the corrosion mean rate. Fig. S12 A displays the values of this rate as measured from *S. oneidensis* WT samples diluted at different initial optical densities $OD_{initial}$, while nanofilms being not connected to any other metals or any electrical connections. The corrosion mean rate does not depend on $OD_{initial}$ and, on average, is found equal to 11 +/- 3 nm/h.

In another manipulation (without electrical connection), we allowed the corrosion process to begin and then we processed to a sudden dilution of the sample by addition of liquid medium. We observed that bacterial dilution neither stopped corrosion nor changed the corrosion rate. In other words, once degradation occurs, its rate doesn't depend on the bacteria concentration, suggesting a corrosion rate not dependent on the number of bacteria at the metal surface.

When nanofilms were connected in series to an ammeter and to a platinum counter-electrode half-immersed from the top of the liquid, we observed that nanofilms degrade much faster with electrical connection than without, as shown in Fig. S12 B. On average, the rate reaches a constant value equal to 17 +/- 3 nm/h. Therefore, the presence of a counter-electrode where only reduction took place increases the corrosion rate.

Interestingly, corrosion rates were measured when nanofilms' corrosion was triggered by different mutants of *S. oneidensis* and by *E. coli* and *L. plantarum* (without electrical connection). Results, which are displayed in Fig. S12 C, indicate a rate independent of the mutants and similar for *E. coli* WT and *S. oneidensis* strains. Only the degradation speed measured on *L. plantarum* differs significantly from the others. These findings point to a reaction independent of the proteins' deletion in the external electron transfers (EET), indicating a corrosion mechanism different from the direct iron-to-microbe electron transfer reported on *Geobacter* species where corrosion pit depth and density strongly depend on the presence of c-cytochromes.[1] The only high rate measured here on *L. plantarum* is most probably related to the low pH (acidic) environment.

From all these findings, we suspect the corrosion phase on iron nanofilm as not being related to *S. oneidensis* – as electron donors to the metal or as electron acceptors from the metal as reported in recent studies (see for instance [2–5]) – but being purely electrochemically activated; bacteria would only enable the passivity breakdown during the initiation phase. That would explain the similar OCP values of the abiotic corrosion of bulk sheet and of the biocorrosion of nanofilms.

Separated compartments

Using a lab-made PTFE two-compartment cell, bacteria were physically separated from the nanofilm by a sterile semi-permeable membrane (12 kDa of pore size, a size sufficient to permeate small secreted molecules like siderophores and small metabolites). Initial conditions: one compartment was filled with a bacterial suspension (2 ml, initial OD= 0.03) and the other (the nanofilm compartment) by sterile liquid medium (about 4.5 ml). At each end of experiments, bacterial contamination in the nanofilm compartment was checked by Optical Density measurement of the separated liquid. Experiments were performed three times on *S. oneidensis* and *E. coli* WT and no corrosion was observed for *S. oneidensis*, unlike *E. coli*. *E. coli* enabled the corrosion transition at identical t_{onset} values using or not separated compartments.

Iron nanofilm processing/preparation

A thorough cleaning of substrates was critical to ensure a perfectly adherent and homogeneous 10-nanometer thick film. To clean glass coverslips (22 mm^2), two protocols were used, both generating the same end result: 1) immersion into an acetone bath with one-minute sonication, then a rinse in isopropanol followed by a second one-minute sonication in an isopropanol bath. Samples were subsequently dried with compressed nitrogen. 2) We manually and actively rubbed the glass substrate with a cotton soaked in CaCO3 dissolved in 3% RBS. Coverslips were then rinsed with distilled water and dried with compressed nitrogen.

To thermally evaporate titanium (Neyco, 99.99%) and iron (Kurt J. Lesker, 99.95%), we placed the glass substrates onto the sample holder of a Plassys evaporator which is located just above two separated tungsten ME5 Neyco crucibles each containing iron and titanium. A quartz balance provided an indication of coating thickness during deposition. The low deposition rate was adjusted within the range 0.08-0.12 nm/s. The decompression phase took place in a nitrogen atmosphere. Then the coverslips were stored in a clean plastic container together with wipes (Kimtech) and exposed to air for a minimum of one to two weeks before use. Delamination and millimeter failure were observed during the manipulation of a few glass coverslips coated less than two weeks before.

Titanium is one of the metals commonly deposited to facilitate other metal adhesion.[6] Iron being deposited on the titanium layer, and being capable of forming stable TiFe or TiFe2 alloys at equilibrium and hot temperature,[7] we cannot exclude the possibility that some iron layers might mix with the titanium film during the deposit. However, measurements of the formation of such an alloy were undetectable by our optical setup. At the beginning of the degradation process, when the signals were accurately measured, kinetic curves and fitted corrosion rates were found to be similar with or without the Ti layer, excluding the presence of such an alloy that would most likely modify the reaction kinetics. However, at the end, when bacterial contribution to the optical signals became relatively high, the low relative precision in the determination of metal thinning might prevent the optical detection of small changes in the completion of metal degradation that would be attributed to the presence of this intermediate layer (TiFe alloy) or simply to the strong adhesion to Ti.

The total number of samples studied in this article is equal to 260, meaning 65 evaporations.

No unexpected or unusually high safety hazards were encountered.

AFM measurements

AFM measurements were conducted in liquid Luria Broth culture media at 23°C using the fast-speed approach/retract mode of the Nanowizard III (JPK Instruments AG, Berlin, Germany) placed on a vibration isolation table. We used CSC37 Cr-AU probes (MikroMasch, https://www.spmtips.com/afm-tip-hq-csc37-cr-au) with a nominal value of stiffness around 0.26 N/m, a value checked before each series of scans by measuring the thermal noise. The approach/retract curves were recorded at a constant speed of 100 µm/s on a vertical 500nm extension range, fixing the maximum applied force value to 5 nN. The surface scanning was

128x128 pixels and we applied a linear smoothing post-treatment to the height AFM images in order to remove the non-horizontality of the sample.

No unexpected or unusually high safety hazards were encountered.

XPS measurements

X-Ray Photoelectron Spectrometry (XPS) was achieved using a K-Alpha spectrometer (Thermofisher Scientific), equipped with a monochromated X-ray Source (Al K_α, 1486.6 eV) of 400 µm spot size. The hemispherical analyzer was operated in CAE (Constant Analyzer Energy) mode, with pass energy of 200 eV and a step of 1 eV for the acquisition of survey (wide-scan) spectra, and pass energy of 20 eV and a step of 0.1 eV for the acquisition of narrow spectra. A "dual beam" flood gun was used to neutralize the charge build-up. At each run, four metal-coated glass coverslips (cleaned with a cloth soaked in ethanol) were analyzed and for each sample, 4-5 survey spectra were first recorded at 5 different positions to map the chemical state of the surface and to check its homogeneity. High resolution spectra in the range of the Fe 2p signal were then repeated several times to check the nanofilms' integrity under vacuum and under the X-ray beam illumination. The chemical state of all detected elements was then determined by fitting the spectra using the casaXPS software. A Shirley type background subtraction was used and the peak areas were normalized using the Scofield sensitivity factors. The peaks were analyzed using mixed Gaussian-Lorentzian curves (70% of Gaussian character) for the case of oxides and an asymmetrical line shape, type LA (1.2,4.8,3)[8] for metallic Fe. Fitting the multiplet splitting[9] was done by the software following the procedure given in [8,10] and establishing area constraints and peak positions. The binding energies were calibrated against the C1s binding energy set at 284.8 eV.

No unexpected or unusually high safety hazards were encountered.

Optical macroscopic measurements

A macroscopic optical setup was mounted using a laser diode source (650 nm of wavelength, Melles Griot) and a photodiode receptor (First Sensor) at the terminals from which we recorded the voltage - high voltage meaning high light level. The diverging light beam emitted from an optical fiber was focalized on the nanofilm while keeping an illuminated area in the order of 1 cm^2, sufficiently large enough to be projected onto the whole photodiode surface. The vertical light propagated first into the liquid medium and then through the nanofilm coverslip (at the bottom of the sample) before being collected by the photodiode.

No unexpected or unusually high safety hazards were encountered.

Electrical measurements.

Electrical measurements were performed using a standard multimeter (Agilent 34410A, internal resistance of $10^{12}\ \Omega$). The external wire was connected to the nanofilm through a platinum connector. Platinum and Ag/AgCl counter-electrodes were purchased from Goodfellow and from Pine Research (distributed by Equilabrium – France) respectively. Note: a negative electrical current was measured under our experimental conditions and only its absolute values are represented in this manuscript for clarity. Once complete nanofilm dissolution occurred (optically measured) and *OCP* measurements were recorded, we noticed the presence of a red species (most likely composed of iron oxides resulting from the nanofilm corrosion) on the porous plug of the Ag-AgCl electrodes altering the exchanges from both sides of the porous plug and incidentally

affecting the post-corrosion *OCP* values. Additionally, a contact area of the nanofilm with the connector remained present which contributed to the *OCP* signal as well.

No unexpected or unusually high safety hazards were encountered.

Microscopic measurements of pH and oxygen (O_2) concentration.

Microsensors (Unisense, Denmark) were used to characterize the local environment of bacteria near the nanofilms. Air-saturated (O_2 = 262.78 μmol/l) and Nitrogen-saturated (O_2 = 0 μmol/l) waters were the two calibration points of the oxygen microsensor (Ox-10 model, outside tip dimension = 8-12 μm) while three classical pH solutions (pH = 4, 7 and 10) were used to calibrate the pH sensor (pH-25 model, outside tip dimension = 20-30 μm). Under an inverted optical microscope (Primovert, Zeiss) and using a manual micromanipulator (Märzhäuser Wetzlar, MM33 right), microelectrodes were set at 30-40 micrometers from the glass coverslips placed at the bottom of the Petri dishes. Spacing calibration was previously done thanks to a motorized linear micropositioning stage (M-126-CG1, PI Physik Instrumente).

No unexpected or unusually high safety hazards were encountered.

Iron Reduction – Ferrozine assay

After the dilution step (previously described), bacteria were allowed to grow up to *OD* ~ 0.3 and were then re-diluted to *OD* = 0.1 into liquid LB supplemented with (7.8 +/- 0.7) mM of soluble iron(III) ammonium citrate (Sigma-Aldrich). Aliquots of 2 ml were prepared and were stored static (without agitation), at room temperature (23°C). After the eppendorf tubes were completely filled and closed, bacteria generated anaerobic conditions within less than 15 minutes. To keep the same conditions for every sample, we did one aliquot per measurement. At each point, bacterial growth was controlled by measuring the *OD*. Then, the aliquot was centrifuged at 12.000 g for 5 min. 100 µl of the supernatant was collected and diluted into 0.5 M HCl. Fe(II) and Fe(III) concentrations were determined using ferrozine assay as described in [11] and calibrated with FeCl2. Note that, instead of a microplate reader, a spectrophotometer (GENESYS™ 40/50 visible / UV-visible) was used to read absorbance (optical densities).

No unexpected or unusually high safety hazards were encountered.

Supplementary Figures

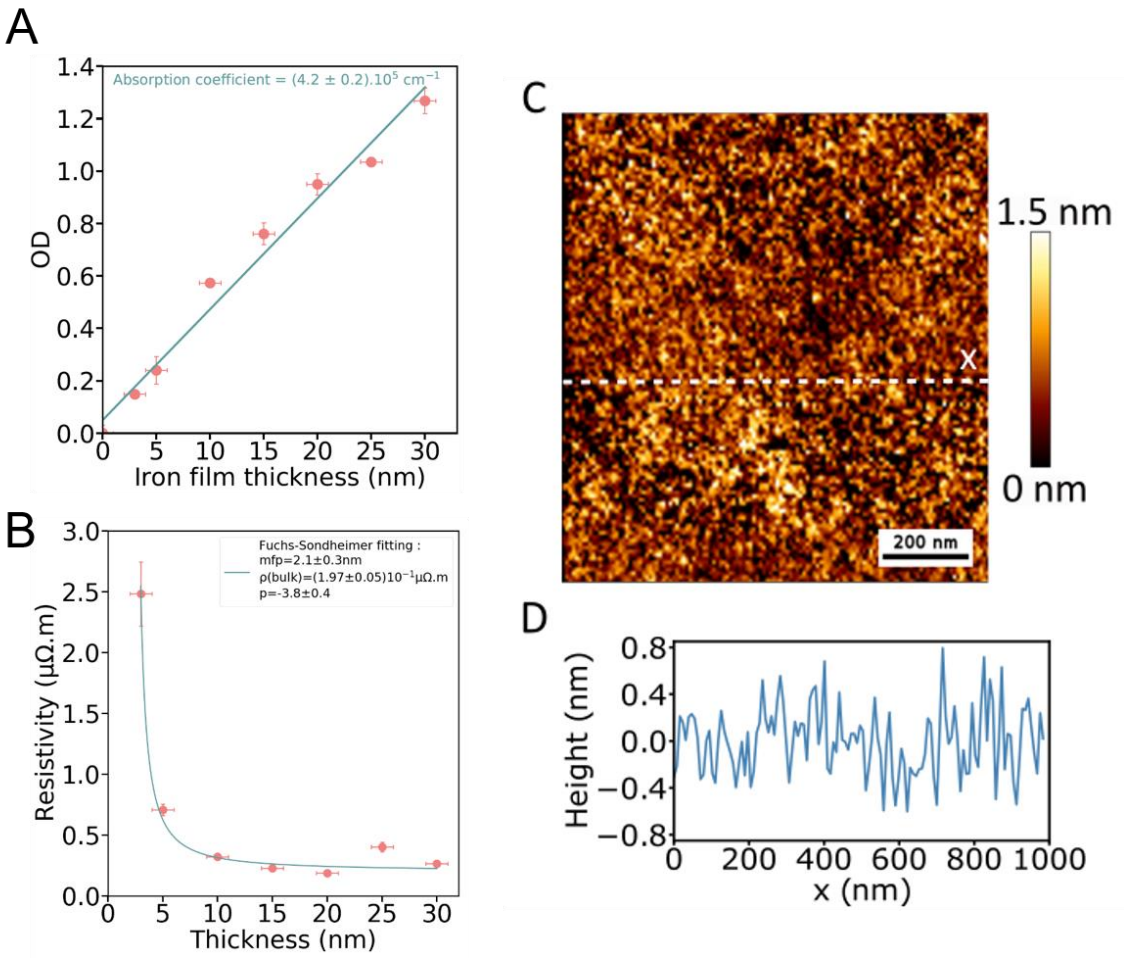

Figure S1. Some physical properties of iron nanofilms. (A) Optical Density of nanofilms as a function of their thickness, iron being thermally evaporated on different glass coverslips without titanium adhesion prelayer. Optical density was directly measured using a commercial spectrophotometer (Genesys 50, Thermoscientific) at a wavelength of 633nm and without liquid. When considering the best linear fit (blue line), the slope provides an experimental value of the absorption coefficient equal to (9.7 +/- 0.4) 10^5 cm^{-1}. This value is close to the optical constant reported in the literature: 6.1 10^5 cm^{-1}.[12-13] Note that surprisingly no change in slope is observed when the iron thickness values reach a few nanometers, which represent the typical thickness of iron oxide overlayers. In this case, the absorption coefficient is expected to be at least ten times smaller than the Fe(0) value, for exemple α = 29202 cm^{-1} for the Fe_3O_4 magnetite.[14] (B) Dependence of the electrical resistivity over the iron nanofilm thickness. Electrical resistivity of iron nanofilms was monitored by a four-point electrical setup without liquid. Four point electrodes were aligned and separated by two millimeters from each other. Current was applied through outer probes and voltage was measured across two inner probes. Resistivity data (pink-filled circles) were deduced from sheet resistance values applying corrective factors 0.943 due to geometry and 4.53 due to ultrathin thickness as described in [15]. The blue curve corresponds to the Fuchs-Sondheimer function that best fits the experimental data;[16] three parameters (*mfp*, ρ, *p*) were

adjusted. The model provides a mean free path of *mfp* = (2.1+/-0.3) nm, which is consistent with the value calculated from the Drude model equal to 3 nm. The value of bulk resistivity extracted from the fit was equal to ρ = 0.20 +/- 0.01 µΩ.m which corresponds to two times the value expected for bulk Fe(0): 0.10 µΩ.m. A similar difference was already observed in ultrathin films.[17] The negative fitted value of the last parameter *p* (*p* = -3.8) corresponding to the fraction of electron specularly scattered from the surface, was thought to be due to the presence of oxygen atoms and of an oxide-metal rugose interface. The irregular interface was thought to be responsible for the electrons scattering.[18] (C) Mapping of nanofilm surface detected by Atomic Force Microscopy where isotropic irregularities and grainy texture were observed. Figure S1 C represents a typical reconstructed image of the scanned surface height (128x128 pixels) in which brightness of each pixel varies with height according to the height scale bar. At each pixel, height is extracted from an approach/retract curve – that is, force-distance curve –, height corresponding to the contact point position. Similar topography images with disordered small irregularities were obtained at different locations on a nanofilm. (D) Profile of the surface height along the white dashed line on Fig. S1 C displays nanofilm roughness. Figure S1 D illustrates a height profile along one axis – along the x dashed white line in Fig. S1 C – and reveals a height dispersion smaller than 0.6 nm over the micrometer horizontal distance; when averaged over the whole image scanned surface, the root mean square roughness equals to 0.4 nm, a value equivalent to the size of few atoms for an image area of 1 x 1 micrometers^2. These values are typical of those obtained from metals thermally deposited at low evaporation rates (around 0.1 nm/s).[19] Nanometric roughness and homogeneity of nanofilms could prevent pinning of corrosion pits as pitting initiation was found strongly dependent on the metal surface condition and usually related to chemical and physical surface inhomogeneities or defects.[20–25]

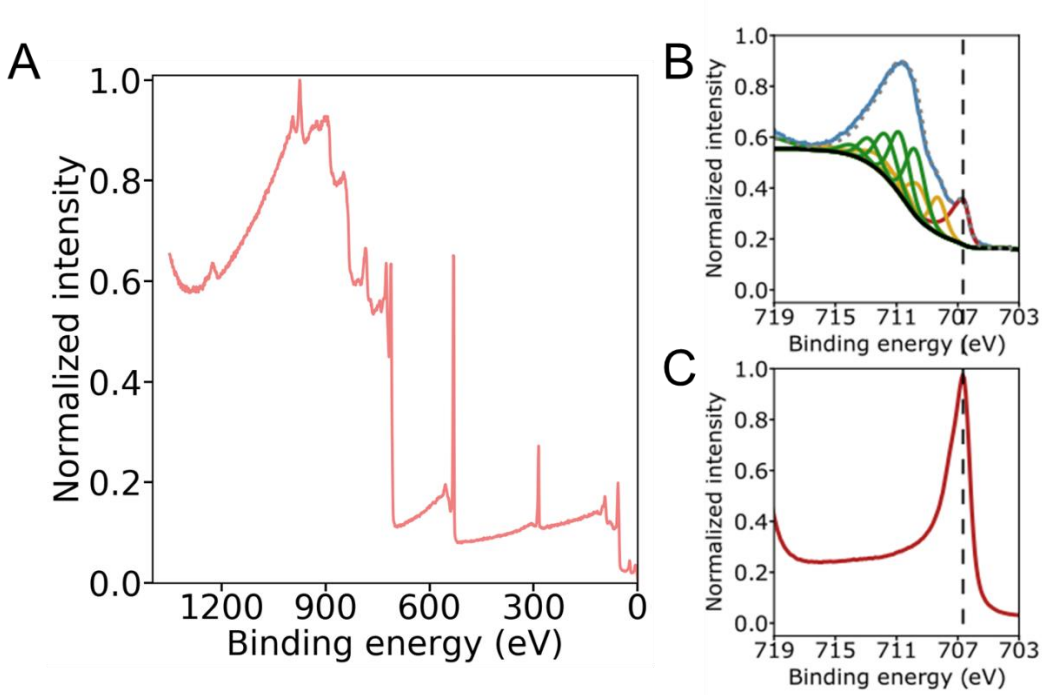

Figure S2. Spectra of X-ray Photoelectron Spectrometry (XPS). Under X-ray irradiation, core electrons are ejected from these surface atoms, captured, and counted according to their energy. (A) Wide-scan spectra of different samples indicated the presence of oxygen (50-70%), iron (20-35%) and carbon (15-25%). Identical results were obtained over different parts of the nanofilms surface demonstrating their chemical uniformity. The presence of carbon elements is attributed to surface contamination as commonly reported for most samples exposed to the atmosphere.[26] (B) Figure S2 B shows further detailed analyses of the iron region Fe2p revealing the presence of Fe(0) (10-20%), FeII (25-30%) and FeIII (50-60%). It clearly suggests that the surface iron overlayer is mainly composed of different oxides/hydroxides/oxyhydroxides, a result confirmed by the presence of oxygen. Note that the oxide grows and covers the surface quite rapidly when exposed to air, being detected on samples evaporated 4 hours before the XPS analysis. We also noticed the fragility of these freshly evaporated samples because they are subject to millimetric hole formation during their manipulation. In contrast, nanofilm samples that were left alone for more than a week after evaporation are mechanically stable. XPS analysis indicates a reduced fraction of Fe(0) compared to the other Fe states, suggesting the existence of a slow oxide growth. (C) Finally, ion etching enabled us to determine the chemical composition of the inner layers. As illustrated in Fig. S2 C, underneath the iron oxide and carbon layer appears a single state, the pure Fe(0) metal. These results are in agreement with [27,28] in which similar nanofilms were studied. Oxidized iron nanolayers overlaying the Fe(0) metal were found non-crystalline and about 3 nm thick. Interestingly, though having a different chemical composition, a similar thin oxidized overlayer (1-3 nm) protects stainless steels from corrosion and is considered to be passive and responsible for their outstanding corrosion resistance.[29] Pure iron metal, however, exhibits a passive oxidized layer that is not stable enough to maintain the passivation state for prolonged time periods.[30]

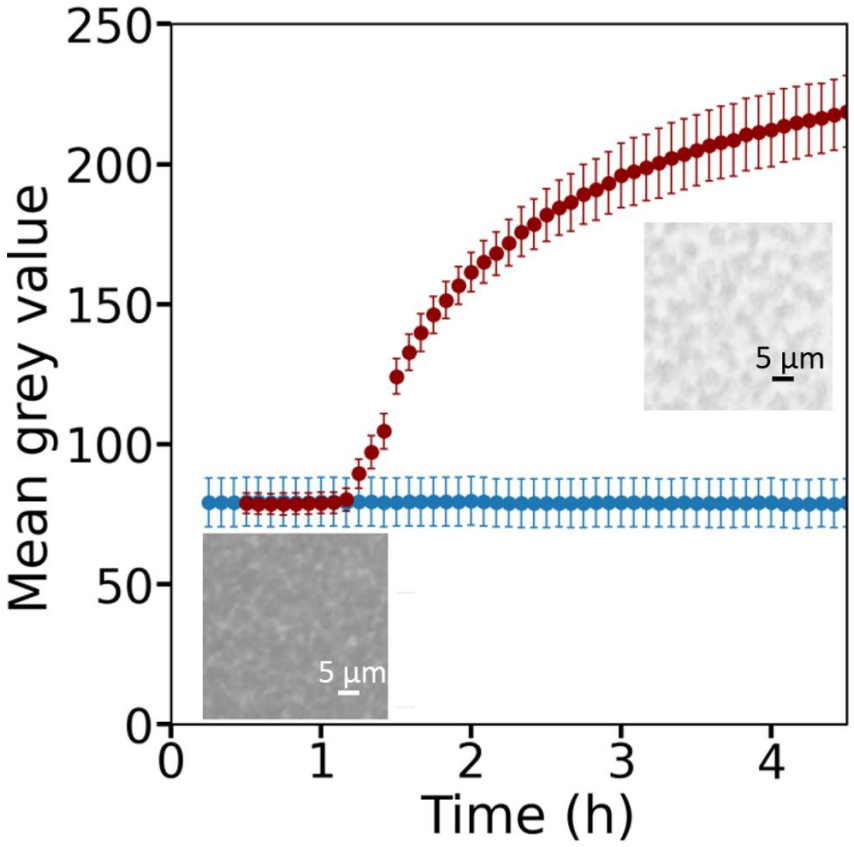

Figure S3. Temporal degradation of a nanofilm in the presence of bacteria (red-filled circles), as observed by optical microscopy. Initial *OD* = 0.07. Figure S3 displays a time variation of the mean grey value (per pixel) together with two images recorded at the beginning and at the end of the experiment. The first dark image contrasts to the last bright image, which reveals without ambiguity the nanofilm corrosion in between, hence validating our approach. Under these experimental illumination and detection conditions, the mean grey value increases from 80 up to 235, a value close to 255 (Black = 0 and white = 255 pixel values of an 8 bit grayscale image). The nonmonotonic increase suggests the existence of a sudden corrosion onset. Moreover, images of intermediate brightness (not shown) present uniform backgrounds indicative of a uniform and homogeneous corrosion. Corrosion above the micron scale would imply localized brightness surrounded by dark areas and consequently, a standard deviation much higher than the low standard deviations represented by the error bars in Figure S3. The standard deviation only increases from 4 to 12 grey levels as it does in samples where bacteria grew without metal deposit, suggesting an increase correlated to the growing number of bacteria (dark features) rather than to degradation heterogeneity. Without bacteria (blue-filled circles), the mean grey value remains constant, meaning no degradation.

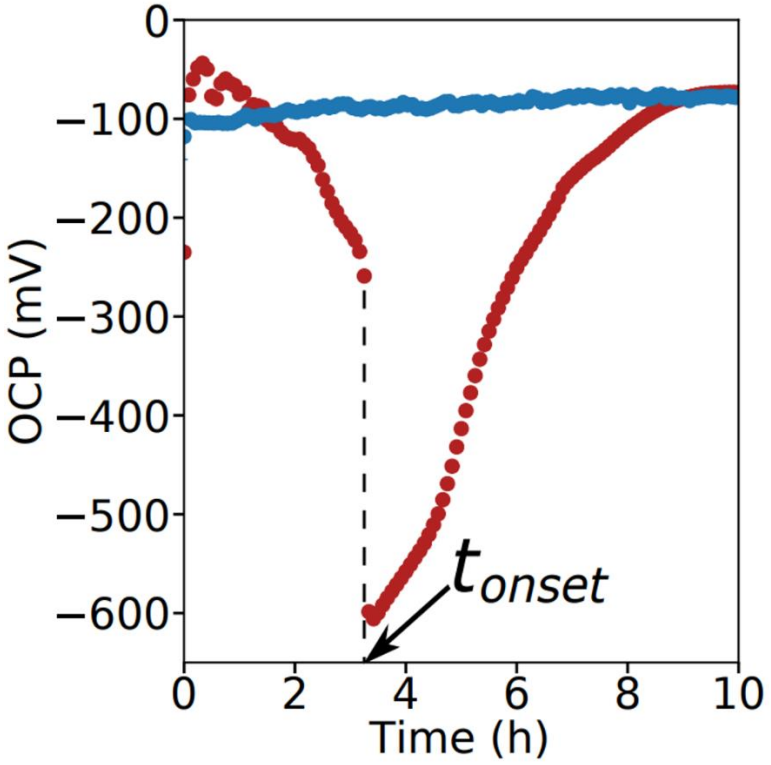

Figure S4. Open Circuit Potential measured during the nanofilm degradation when connecting the iron nanofilm to a voltmeter and to a Ag/AgCl reference electrode (as a counter-electrode). A sudden drop from - 200 mV to -600 mV appeared at the beginning of the corrosion process (red-filled circles). Initial *OD* = 0.03. Other constant electrical signals were measured on an Fe nanofilm immersed into the abiotic liquid medium without bacteria (blue-filled circles). All the electrical measurements were done on iron nanofilms evaporated directly on glass coverslips (without Ti layer).

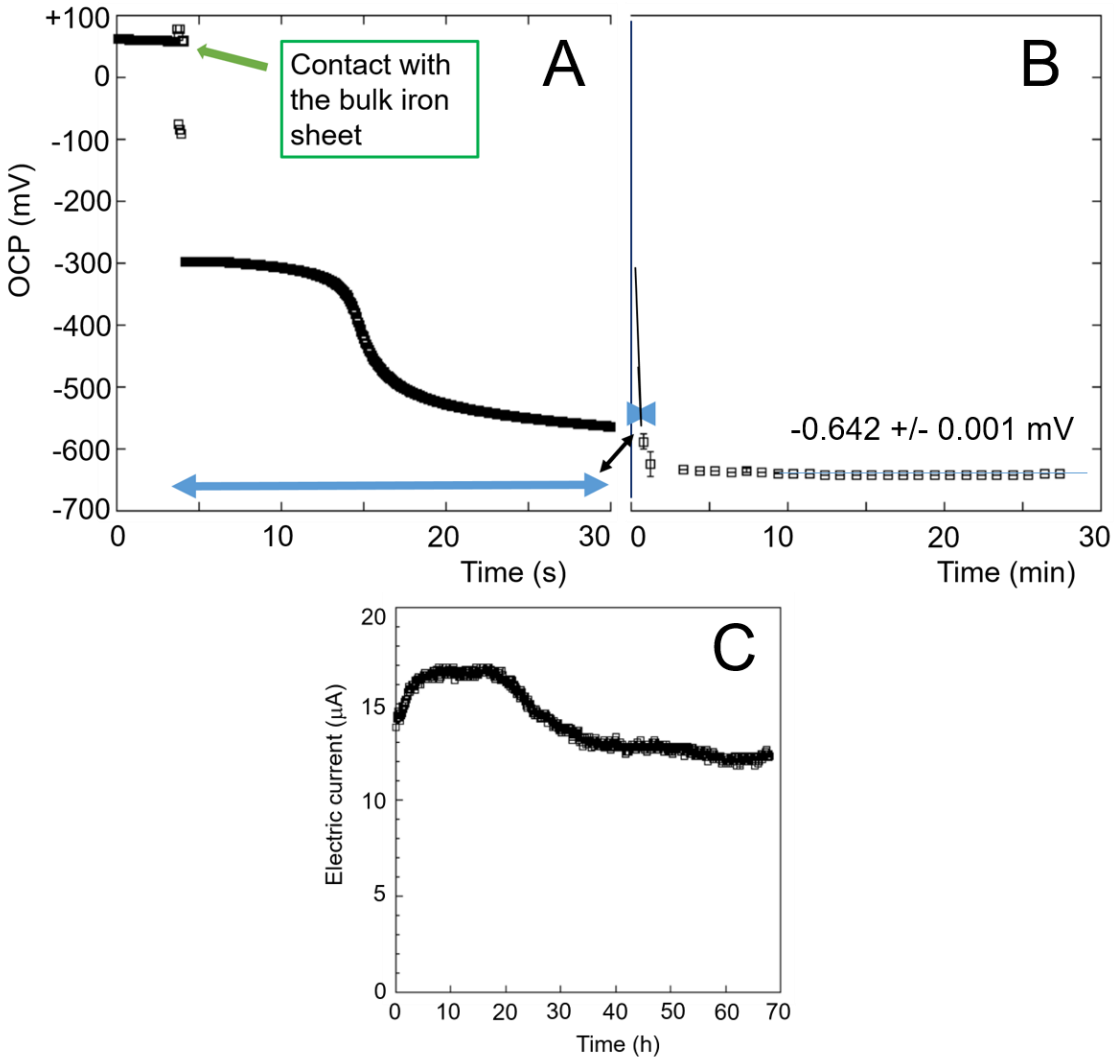

Figure S5. Electrical signals measured during the bulk iron degradation and using a Ag/AgCl counter-electrode**.** Two bulk iron sheets (0.1 mm-thick, GoodFellow, Iron 99.5%) were each immersed into two separate abiotic LB media at time *t = 0* without bacteria. The temporal variation of the *OCP* (Open-Circuit Potential) measured on the first sample is shown in (A-B). Horizontal time axes are expressed in second (A) and minute (B) units to display the short and long-time variations. Two kinetics were observed: the OCP values initially dropped to -300 mV when connecting the electrical circuit to the iron sheet (contact) (A) and then decreased to - 642 mV after one or two minutes (A-B). (C) The electric current resulting from the bulk iron degradation of the second sheet was measured over a period of three days. The absolute values, displayed in Fig S5 C, are of the order of 15 µA. Data suggest a rapid instability of the oxide covering the bulk metal and a corrosion starting quasi-immediately after immersion.

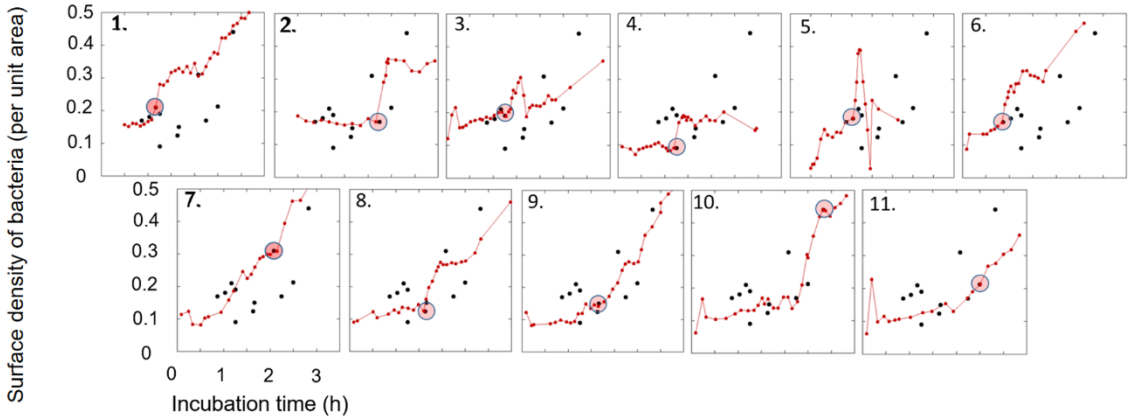

Figure S6. Temporal variations of bacterial surface density (per unit area) as functions of time measured by processing the digital images recorded by optical microscopy on eleven samples. Images were treated and analyzed using Python programs.[31,32] Bacteria were extracted from the background by searching features of variable pixel intensity and of given size or area. Among the different applied methods, all rendering the same results, the segmentation and binarization techniques described in [33] allowed us to unambiguously determine the area covered by bacteria. Densities σ_S (red-filled circles) were calculated by counting the total surface areas occupied by bacteria per unit area. For each sample, corrosion onset t_{onset}, determined by analyzing simultaneously variations of the mean grey values, is marked by a semi-transparent red disk. On each plot, all the coordinate points (t_{onset}, σ_S^{onset}) determined from imaging of all samples are also marked by the black-filled circles. Three plots (4., 5., 6.) display data obtained from the iron nanofilms directly evaporated on glass without an adhesive Titanium layer. A titanium layer was deposited under the iron layer of the other samples. Plot (2.), initial *OD*= 0.03; the others, *OD*= 0.07.

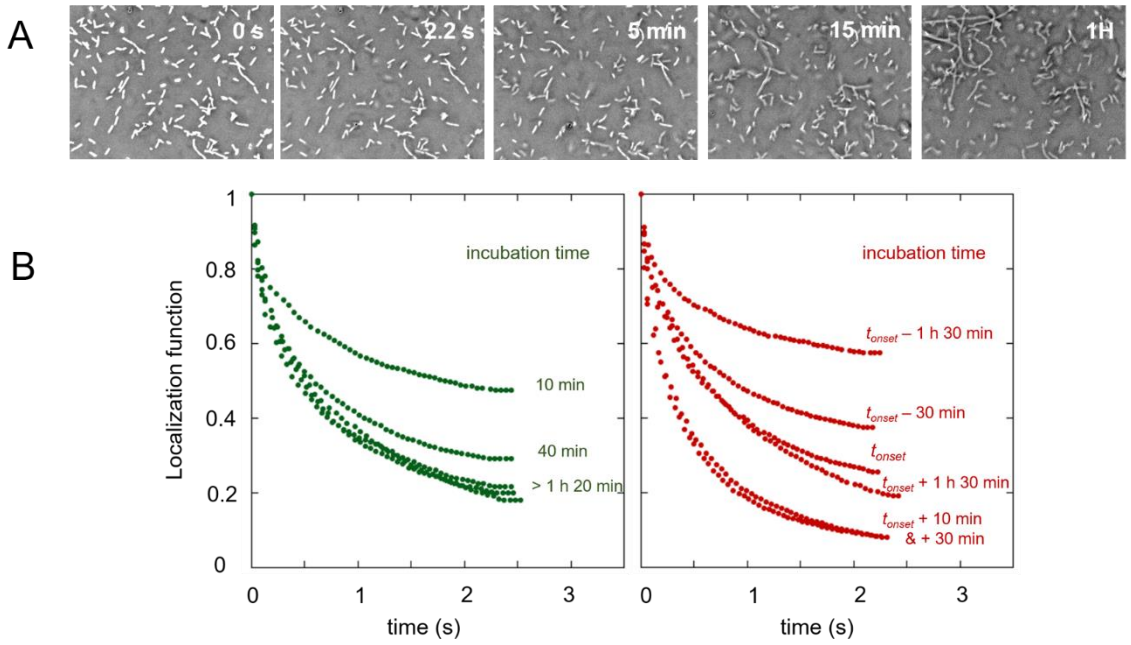

Figure S7. Cells' dynamics and sessility analysis. (A) Visualization of cells or any immobile part for long periods of time. The first image on the left side was obtained by processing the image recorded at an initial moment, noted *t*= 0 sec. The first and second images correspond to the first and last images of a 50-picture sequence lasting 2.2 seconds. In the first, bacteria detected by the program appear white-colored and simply overlaid onto the initial image. As can be seen, all cells have been detected. The second was reconstructed differently: only pixel sites occupied by the same immobile bacteria within the 50 previous images appear white-colored. Once a pixel grayscale level changed from one picture to another (due to bacterial motion) its grayscale level was converted to a zero background level. By comparing the pixel values from one image to the next in the sequence and annealing successively their level, the result (second image) contains only white-colored pixel sites in which no motion was detected during the entire sequence analysis; the rest of pixels were considered as background and transparent. Therefore, the binary overlaying image only enhances the contrast of cells or any part that remained immobile during the 50 previous images *i.e.* during 2.2 seconds. Similar enhancement was applied to three other images recorded at 5 min, 15 min and 1 hour after the initial moment. (B) Quantitative analysis of bacterial immobility based on a localization function. To quantify temporal distribution of displacements that extended from milliseconds to hours, we analyzed how bacteria moved from initial sites or equivalently how bacteria or part of bacteria continued to reside on these initial sites. The relative total area of initial sites that were still occupied at any time *t* after the initial moment ($t_{initial} = 0$) is termed the localization function; the function equals 1 or 0 when initial sites are all still occupied (no motion at all) or abandoned, respectively. For practical purposes, we restricted our analysis to the first seconds that followed the initial moment. The functions analyzed on the two samples of Fig.4B are plotted here versus time. The reference sample where bacteria resided on a glass substrate is considered on the left-hand graph (green-filled circles). The different curves in this plot were calculated starting from different initial states i.e. from states recorded at different incubation times. Thus the upper curve describes the situation in which bacteria were initially localized on the surface 10 minutes after bacterial inoculation. Progressively, the function decreases at varied characteristic times attributed to multiple bacterial motions. Within 150 ms, an initial rapid decrease from 1 to 0.8 was recorded, followed by a slowing decay between 0.8 and 0.5. By decomposing the motions observed on the images' sequence, we attribute the first decrease to local fast runs of bacteria swimming in

the liquid near the glass surface within the 20 μm depth of observation field; we deduced a 20% fraction of running bacteria. The second part of the curve deals therefore with non-running cells, the cells that seemed immobile long-term. Two processes contribute to the decreasing function: 1) a progressive thinning of each localized site area induced by local small displacements and attributed to constrained thermal motions on the surface 2) sudden extinctions of large areas due to large motions of bacteria like removal/detachment or large reorientation. The function reached the 0.5 value after only a few seconds; this being the largest value observed when analyzing localization persistence at different incubation times, meaning the earliest surface bacteria remained localized and motionless for the longest period of time. Surprisingly, after 1 hour 20 minutes (1 h 20) of incubation, the curves superimposed and it became difficult to separate the contribution of each kind of motion to the ratio. Bacteria became more concentrated at long incubation times and subject to thermal motions. The other graph on the right-hand side (red-filled circles) displays the temporal variation function when bacteria were in contact with a metal nanofilm. The different initial states are indicated according to their temporal proximity to the corrosion onset – not to be confused with the incubation time. During the initiation phase (negative time), the curves were similar to the previous recorded on samples without metal, pointing to the absence of any specific interactions or affinities with the substrate that would have modified bacteria localization and dynamics during this phase. Similarly, after the corrosion process (more than one hour after the onset), the curve converged with the curve recorded before the onset i.e. to a hypothetical unique curve as previously noted. The only differences clearly observed were in the first minutes and ten minutes just after the corrosion onset. The function rapidly decreased and reached about 0.8 and 0.2, just 0.1 and 1 second after the initial state, respectively. Therefore, as seen in Movie S1, each bacterium was highly dynamic and all local motions were rapid; no cells were motionless meaning a complete and immediate delocalization. Their instantaneous velocities are discussed in the main text.

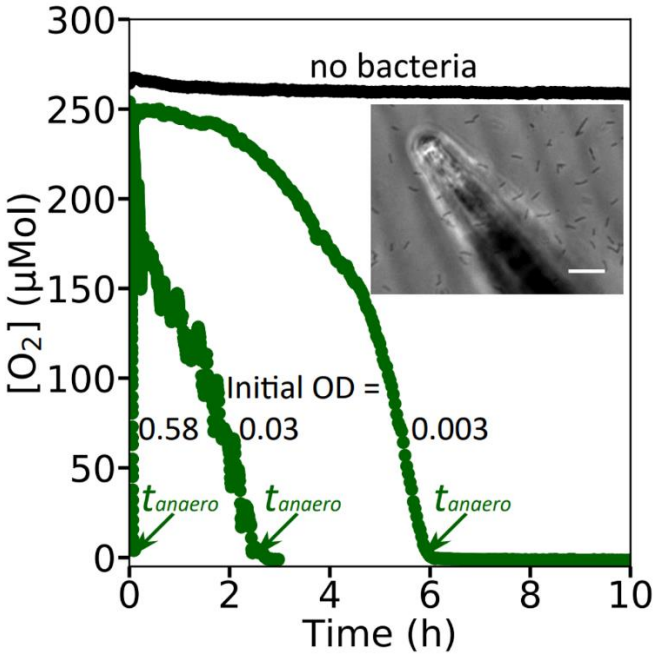

Figure S8. Kinetics of oxygen (O_2) depletion measured using a microelectrode on four samples: the medium itself without bacteria and three bacterial cultures of different initial concentrations ($OD_{initial}$ = 0.003, 0.03 and 0.58). As shown in the insert (scale bar = 20 μm), the microelectrode was lowered to the bacteria located at the sample bottom (at 20-50 micrometers from the surface). Bacteria consumed dissolved oxygen (O_2) and generated an anaerobic environment after a certain time period.[34] The different times, t_{anaero} marked by green arrows indicate when oxygen was locally fully-depleted.

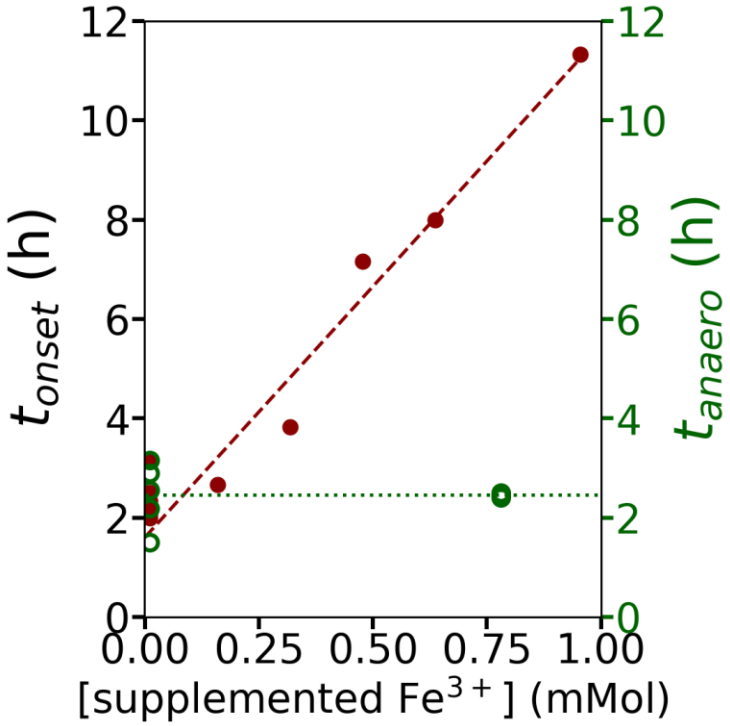

Figure S9. Delay in the corrosion onset upon addition of soluble Fe(III). Supplementing the medium with Fe(III) ammonium citrate strongly delayed the corrosion event (t_{onset}, red-filled circles, right vertical axis) without perturbing the bacterial O_2 consumption (t_{anaero}, green-filled circles, left vertical axis). The initial *OD* value (= 0.03) was kept constant. Dashed lines represent linear (red) and constant (green) fits.

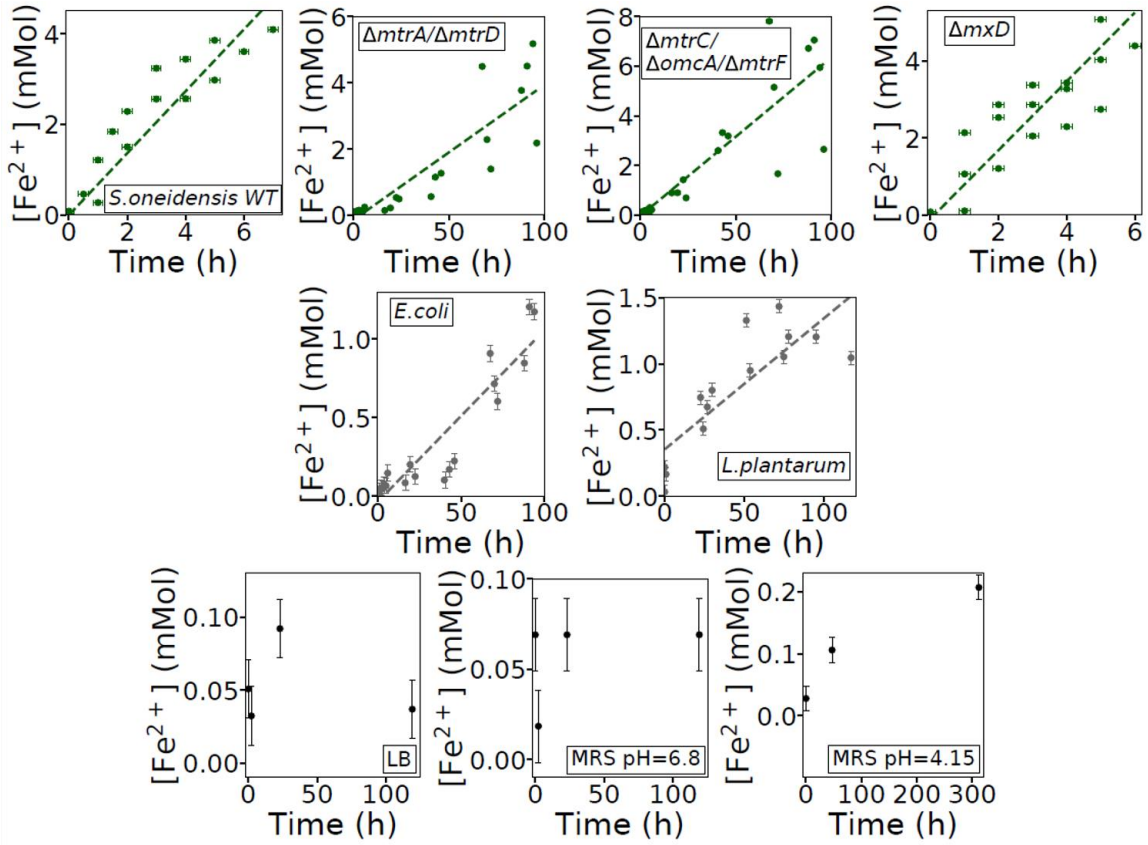

Figure S10. Kinetics of iron(III) reduction. Thanks to ferrozine assay, iron (II) concentrations in samples from three different bacterial species were measured at incubation times ranging from 6 to 100 h. Each sample initially contained (7.8 +/- 0.7) millimolars of iron(III) citrate with initial *OD* = 0.10. The data sets of *S. oneidensis* MR-1 and its three mutants (previously described) were plotted in the first row (green-filled circles). For each strain, the reduction rate k_{reduc} was extracted from the slope of the best affine fit (green line), leading to: (0.68+/-0.01) mM/h, *S. oneindensis* WT; (0.041+/-0.001) mM/h, *ΔmtrA/ΔmtrD*; (0.064+/-0.001) mM/h, *ΔmtrC/ΔomcA/ΔmtrF*; (0.89+/-0.02) mM/h, *ΔmxD*. These values are in agreement with those reported in the literature.[35,36] Iron reduction was related to the lifestyle of *Shewanella.*[11] In the second row, plots render measurements performed on *E. coli* and *L. plantarum* samples (grey-filled circles) with the best affine fits (grey lines) leading to k_{reduc}= (0.011+/-0.001) mM/h, *E coli* and (0.0098+/-0.0004) mM/h, *L. plantarum*. Similar iron (II) concentration measurements were done on sterile culture media as controls and are plotted in the third row (black filled circle). LB culture medium was used to culture *S. oneidensis* and *E. coli*, and MRS was used to culture *L. plantarum*, both being set at nearly neutral pH (6 – 7.5). As *L. plantarum* acidified its environment, a control of iron III reduction under acidic conditions (pH=4.15) was also performed. Here, residual iron II molecules (0.05-0.1-0.2 mM) were found over large periods of time.

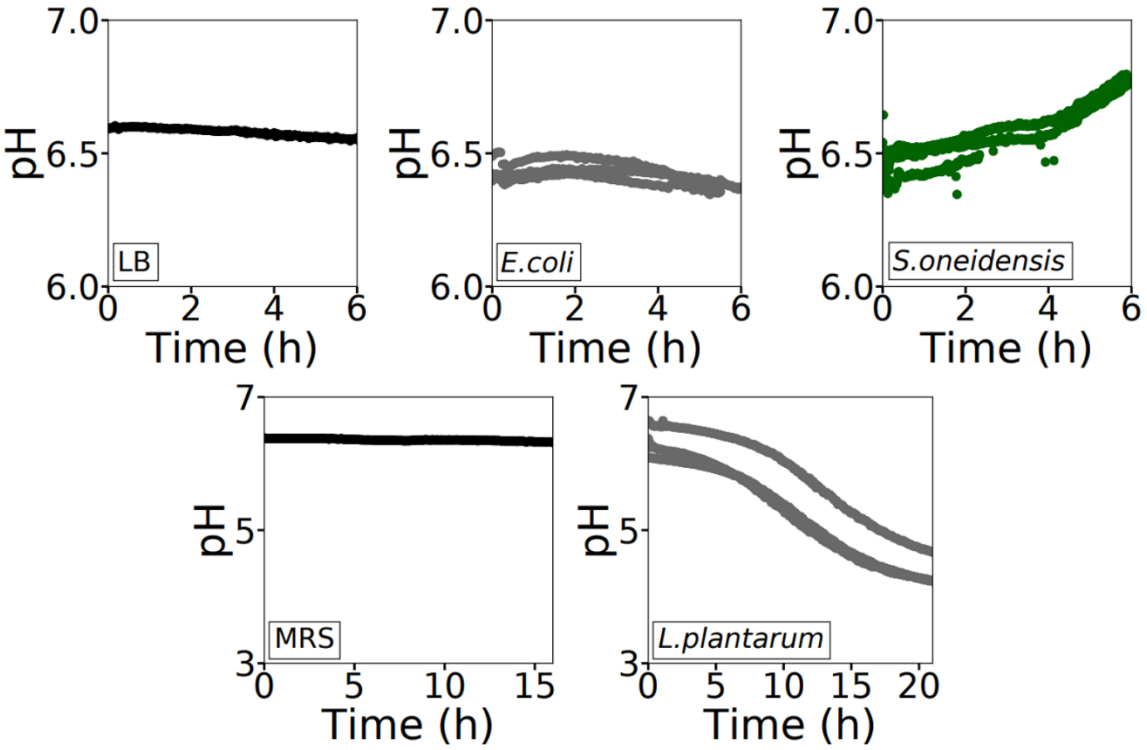

Figure S11. Temporal variations of local pH as measured using a microelectrode positioned at 20-50 µm from the bottom glass coverslip surface, a situation similar to the previous case (local oxygen levels on Figure S6). Five plots are presented, three data series recorded from three different bacterial species, *S. oneidensis* (green-filled circles), *E. coli* and *L. plantarum* (gray-filled circles) and two from two different culture media without bacteria (black-filled circles). The latter pH values remain constant over time with values around 6.5 +/- 0.05 for LB and 6.35 +/- 0.02 for MRS. A constant value was also observed for *E. coli* samples with a mean pH value of 6.37 +/- 0.7. Furthermore, *S. oneidensis* samples exhibited a slow pH increase from 6.35 to 6.81 over a 6-hour incubation period with a mean value of 6.54+/-0.07. Conversely, a clear decrease was measured on *L. plantarum* samples from 6.65 to 4.12 over 21 hours most likely due to its fermentative metabolism which tends to acidify the culture media. The initial *OD* was 0.03 for each bacterial samples.

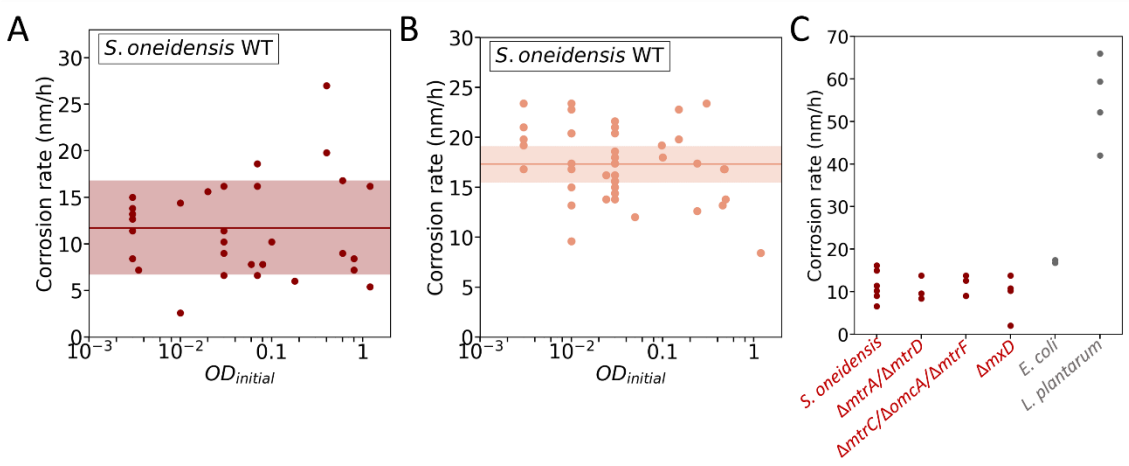

Figure S12. Corrosion rates. Kinetics of nanofilm thinning were adjusted by linear decreasing functions in order to obtain corrosion rate values (straight line in Fig. 2B). (A) *S. oneidensis WT*. A log-lin plot showing corrosion rate values independent of initial bacterial concentration or of optical density $OD_{initial}$. On average, the rate was equal to 11 +/- 3 nm/h (Mean and Standard Deviation illustrated by the horizontal-colored line and the color-filled rectangle respectively). (B) *S. oneidensis WT*. Corrosion rate *vs.* Initial OD. Connection of the iron nanofilm to a Platinum counter-electrode via an external electrical circuit induces faster thinning than without electrical connection. On average, the rate became equal to 17 +/- 3 nm/h. (C) Corrosion rate values were extracted from kinetics measurements of the three mutants of *S. oneidensis* (*ΔmtrA/ΔmtrD*, *mtrC/ΔomcA/ΔmtrF* and *ΔmxD,* red-filled circles) and of the two bacterial species (E. *coli* and *L. plantarum*, gray-filled circles). *S. oneidensis*, as noted alone, refers to the WT strain. The initial *OD* was set to 0.03 for each bacterial sample.

Legend for Movie S1 (separate file). A one-looped and slow motion movie showing six sequences of 50 images recorded before and during the corrosion of the same sample (t_{onset} = 1 h 40). Microscopic observations of the nanofilm surface were performed within the 20 μm depth observation field**.** Brightness of the grayscale images was kept constant by image processing (thresholding and renormalization)[31] in order to facilitate the bacteria observation. In this sample, bacterial influx, quantified by non-monotonic variation of the surface density illustrated in the right plot Fig. 3B, was clearly seen less than ten minutes after the corrosion onset. As observed on all samples, bacteria exhibited rapid motions after t_{onset}, likely due to iron release. (Image scale given in Fig. 3A). Initial *OD* = 0.07.

SI References

1. H.-Y.Tang, C. Yang, C., Ueki, T. et al. Stainless steel corrosion via direct iron-to-microbe electron transfer by *Geobacter* species. *ISME J* (2021). https://doi.org/10.1038/s41396-021-00990-2
2. D.E. Ross, J.M. Flynn, D.B. Baron, J.A. Gralnick, D.R. Bond, Towards Electrosynthesis in *Shewanella*: Energetics of Reversing the Mtr Pathway for Reductive Metabolism. *PLoS ONE* 6, e16649 (2011).
3. A.R. Rowe, P. Rajeev, A. Jain, S. Pirbadian, A. Okamoto, J.A. Gralnick, M.Y. El-Naggar, K.H. Nealson. Tracking electron uptake from a cathode into Shewanella cells: implications for energy acquisition from solid-substrate electron donors. *mBio* 9, e02203-17 (2018).
4. R.B. 2nd Miller, K. Lawson, A. Sadek, C.N. Monty, J.M. Senko. Uniform and Pitting Corrosion of Carbon Steel by Shewanella oneidensis MR-1 under Nitrate-Reducing Conditions. *Appl Environ Microbiol.* 84, e00790-18 (2018).
5. J. Philips, N. Van den Driessche, K. De Paepe, A. Prévoteau, J.A. Gralnick, J.B.A. Arends, K. Rabaey. A novel Shewanella isolate enhances corrosion by using metallic iron as the electron donor with fumarate as the electron acceptor. *Appl Environ Microbiol* 84, e01154-18 (2018).
6. D. M. Mattox, Handbook of Physical Vapor Deposition (PVD) Processing: Film Formation, Adhesion, Surface Preparation and Contamination Control (Noyes Publications, Park Ridge (New Jersey), 1998).
7. T. B. Massalski, H. Okamoto, P. R. Subramanian, L. Kacprzak, Binary alloy phase diagrams (ASM international, 2nd ed., USA, 1990).
8. M. C. Biesinger, B. P. Payne, A. P. Grosvenor, L. W. M. Lau, A. R. Gerson, R. St. C. Smart, Resolving surface chemical states in XPS analysis of first row transition metals, oxides and hydroxides: Cr, Mn, Fe, Co and Ni. *Appl. Surf. Sci.* 257, 2717-2730 (2011).
9. R. P. Gupta, S. K. Sen, Calculation of multiplet structure of core p-vacancy levels.II. *Phys. Rev. B.* 12, 15-19 (1975).
10. I. S. Molchan et al., Microscopic study of the corrosion behaviour of mild steel in ionic liquids for CO2 capture applications. *RSC Adv.* 5, 35181 (2015).
11. J. Yuan, Y. Chen, G. Zhou, H. Chen, H. Gao, Investigation of roles of divalent cations in Shewanella oneidensis pellicle formation reveals unique impacts of insoluble iron. *Biochim. Biophys. Acta*, 1830, 5248 (2013).
12. M. N. Polyanskiy, "Refractive index database". https://refractiveindex.info. Accessed on 2021-03-10.
13. P. B. Johnson, R. W. Christy, Optical constants of transition metals: Ti, V, Cr, Mn, Fe, Co, Ni, and Pd. *Phys. Rev. B* 9, 5056-5070 (1974).
14. M. R. Querry. Optical constants, Contractor Report CRDC-CR-85034 (1985).
15. Ossila. 2021. https://www.ossila.com/pages/sheet-resistance-theory.
16. K. Fuchs, The conductivity of thin metallic films according to the electron theory of metals. *Math. Proc. Cambridge Philos. Soc*. 34, 100108 (1938).
17. R. Singh, A. Surplice, The electrical resistivity and resistance-temperature characteristics of thin titanium films. *Thin Solid Films* 10, 243-253 (1972).
18. D. Dayal, P. Rudolf, P. Wibmann, Thickness dependence of the electrical resistivity of epitaxially grown silver films. *Thin Solid Films* 79, 193-199 (1981).
19. N. Mahmoodi, A. I. Rushdi, J. Bowen, A. Sabouri, C. J. Anthony, P. M. Mendes & J. A. Preece, Room temperature thermally evaporated thin Au film on Si suitable for application of thiol self-assembled monolayers in micro/nano-electro-mechanical-systems sensors. *J. Vac. Sci. Technol. A* 35, 041514 (2017).
20. Y. Wang, G. Cheng, Y. Li, Observation of the pitting corrosion and uniform corrosion for X80 steel in 3.5% NaCl solutions using in-situ and 3D measuring microscope. *Corr. Sci.* 111, 508-517 (2016).

21. D. D. Macdonald, Passivity – the key to our metals-based civilization. *Pure Appl. Chem*. 71, 951-978 (1999).
22. V. Maurice et P. Marcus, Progress in corrosion science at atomic and nanometric scales. *Prog. Mater. Sci*. 95, 132-171 (2018).
23. C. Punkt, M. Bölscher, H. H. Rotermund, A. S. Mikhailov, L. Organ, N. Budiansky, J. R. Scully, J. L. Hudson, Sudden onset of pitting corrosion on stainless steel as a critical phenomenon. *Science* 305, 1133 (2004).
24. H. Khachatryan, S.-N. Lee, K.-B. Kim, and M. Kim, Deposition of Al Thin Film on Steel Substrate: The Role of Thickness on Crystallization and Grain Growth. *Metals* 9, 12 (2019).
25. G. T. Burstein, C. Liu, R. M. Souto, S. P. Vines, Origins of pitting corrosion. *Corros. Eng. Sci. Technol*. 1, 39 (2004).
26. ThermoFisher Scientific. https://xpssimplified.com/elements/carbon.php
27. M. D. Boamah, E. H. Lozier, J. Kim, P. E. Ohno, C. E. Walker, T. F. Miller III, F. M. Geiger, Energy conversion via metal nanolayers. *Proc. Natl. Acad. Sci. U.S.A* 116, 16210-16215 (2019).
28. D. Faurie-Wisniewski, F. M. Geiger, Synthesis and characterization of chemically pure nanometer-thin zero-valent films and their surfaces. *J. Phys. Chem. C* 118, 23256-23263 (2014).
29. C.-O. A. Olsson, D. Landolt, Passive films on stainless steels – chemistry, structure and growth. *Electrochim. Acta* 48, 1093-1104 (2003).
30. T. Ohtsuka, in Characterization of corrosion products on steel surfaces, Y. Waseda, S. Suzuki, Eds (Springer, Berlin, Heidelberg, 2006), pp 19-31.
31. S. van der Walt, J. L. Schönberger, J. Nunez-Iglesias, F. Boulogne, J. D. Warner, N. Yager, E. Gouillart, T. Yu and the scikit-image contributors. Scikit-image: Image processing in Python. *PeerJ*. 2, e453 (2014).
32. J. C. Crocker, D. G. Grier, Methods of Digital Video Microscopy for Colloidal Studies. *J. Colloid Interf. Sci*. 179, 298–310 (1996).
33. J. Bois, G. Chure. 2016. http://justinbois.github.io/bootcamp/2016/lessons/l39_segmentation.html
34. M. Ardré. Dynamique de formation des biofilms de Bacillus subtilis à l'interface eau-air : expériences et modélisation, thesis, Université Paris Sud - Paris XI, France (2014).
35. Q. Wang, A.-A. D. Jones III, J. A. Gralnick, L. Lin, C. R. Buie, Microfluidic dielectrophoresis illuminates the relationship between microbial cell envelope polarizability and electrochemical activity. *Sci. Adv. 5*, eaat5664 (2019).
36. D. Coursolle, J. A. Gralnick, Modularity of the Mtr respiratory pathway of *Shewanella oneidensis* strain MR-1. *Mol. Microbiol.* 77, 995-1008 (2010).